An implicit Material Point Method for micropolar solids undergoing large deformations

Ted J. O'Hare [a], Panos A. Gourgiotis [b], William M. Coombs [a],*, Charles E. Augarde [a]

[a] Department of Engineering, Durham University, South Road, Durham, DH1 3LE, UK
[b] Mechanics Division, National Technical University of Athens, Zographou, GR-15773, Greece

GRAPHICAL ABSTRACT
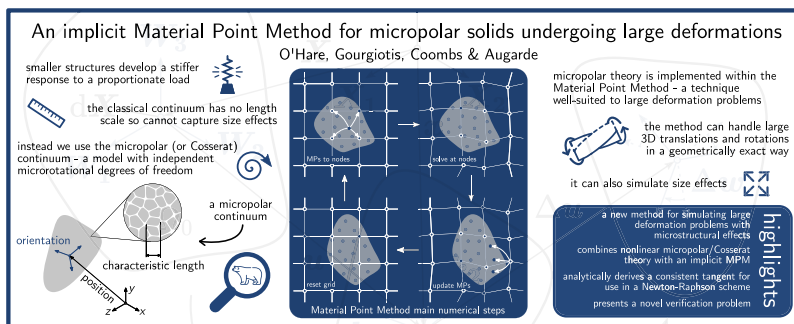
ARTICLE INFO

ABSTRACT

Modelling the mechanical behaviour of structural systems where the system size approaches that of the material microstructure (such as in MEMS) presents challenges to the standard continuum assumption and classical models can fail to predict important phenomena. Of the various non-conventional continuum frameworks developed to tackle this issue, the micropolar (Cosserat) continuum is widely acknowledged as a suitable and rigorous alternative for its ability to naturally predict size effects by introducing characteristic length scales. This work proposes an implementation of geometrically non-linear micropolar theory using an implicit Material Point method, for the purpose of simulating nanoscale large-deformation problems involving Hookean materials. The framework employs an analytically-derived consistent tangent, and is verified with a novel benchmark problem derived using the Method of Manufactured Solutions. Due to similarities between the methods, many aspects of the formulation could be used to construct an Updated Lagrangian Finite Element Method.

---

* Corresponding author.
   E-mail address: w.m.coombs@durham.ac.uk (W.M. Coombs).

1. Introduction

All engineering structures are themselves made of smaller structures. The constituent units (such as metal crystals or polymer chains) are so small and inconsequential, however, that the structure can usually be assumed to comprise completely continuous matter: the so-called *continuum assumption*. This is generally a reasonable pretence, and is one of a number of simplifications made to formulate the classical continuum theories used almost universally to model and design real-life structures. That said, when the overall structural scale is small enough that it approaches that of the microstructure, as is the case in many contemporary miniature industrial applications like microelectromechanical systems (MEMS), wearable electronics and nanoparticle technology, salient size effects in terms of hardness, stiffness and toughness are observed (see e.g. [1]) and conventional models are rendered invalid. A different approach is required [2]. Explicitly modelling a body as an assembly of discrete particles, however, entails significant difficulties, including great computational cost. A more pragmatic approach, and remaining in a familiar continuum mechanics paradigm, is to use a non-conventional continuum theory which offers information about the material microstructure, particularly when it is cellular, crystalline or granular in nature [3].

The idea of a generalised continuum was first conceived for crystalline materials in the latter part of the 19th Century by Voigt [4]. Because Voigt's theory includes couples (moments), and therefore violates the Boltzmann(-Hamel) 'axiom' stipulating the symmetry of the Cauchy stress tensor [5, p. 326], it is classified as a member of the family of *non-Boltzmann* formulations. Micropolar theory is another member, and may be considered an extension of Voigt's couple-stress elasticity. The theory was proposed in a primitive form by the Cosserat brothers in 1909 [6], and was further developed by Eringen, Mindlin and others over half a century later [7–11]. It was generally regarded as too obscure for much practical use, though, until Mühlhaus and Vardoulakis discovered its ability to predict localised failure zones (shear bands) of finite thickness in soils [12] — at the time an open problem in geomechanics. The regularisation of localisation problems, although outside the scope of this work, is now recognised as one of the theory's main potentials.

Fundamentally, the micropolar model is based on the inclusion of independent microrotations so that, in three dimensions, there are six degrees-of-freedom: three translations and three rotations. The gradient of the microrotations, or *curvature*, is included as a deformation measure, classifying the theory as higher-order and weakly non-local, and requiring the existence of couple-stresses (moments or torques per unit area) for conjugacy. The theory also introduces the idea of characteristic length scales, as constants with the dimension of length appear in the constitutive relationship between the microrotations and couple-stresses. It is through this mechanism that the stiffness of a micropolar continuum directly depends on the relative size of the overall structure to characteristic lengths — the size effect, in other words. Although their physical meaning is the subject of debate, recent studies provide an account of the determination of the characteristic length scales of micropolar theory and related gradient theories via homogenisation of heterogeneous materials (see e.g. [13–16]). They are also often intuitively taken to be indicative of the size of the microstructure, e.g. the diameter of one particle within a nanoparticle assembly. The independent rotation field, which is not directly coupled to the displacements (or therefore to the continuum macrorotation) also particularly qualifies the theory for modelling granular media, in which individual particles have been observed to rotate relative to each other and exert moments [12,17]. Whereas other non-local formulations generally include non-rigorous dependencies or parameters which must be determined by trial and error, crucially all elements of micropolar theory are derived from thermodynamic principles and have a physical basis in structured, oriented media [13].

Numerical implementations of the micropolar continuum first emerged in the 1990s beginning with a Finite Element Method (FEM) developed by de Borst [18,19], following the renewed interest in the theory as a regularisation technique. In the decades since, linearised micropolar theory has been implemented within FEMs for a variety of purposes (e.g. [20–25]), but to the best of the authors' knowledge only a handful of examples using the three-dimensional geometrically-exact non-linear theory exist [26–28],[1] building on its well-established mathematical foundations [31–33]. Of these, only Erdelj et al. [28] considered purely *geometric* non-linearity, formulating a Total Lagrangian (TL) FEM with the classical linear isotropic micropolar constitutive laws.

But despite the fact the FEM has become the tool of choice for analysis of solid mechanics problems, it can suffer from numerical errors due to mesh distortion when modelling large deformations [34]. One solution would be to remesh the entire domain, but this usually engenders numerical difficulties, particularly surrounding projection of history and field variables and computational cost. Instead, alternative numerical methods which are not solely mesh-based may be employed, such as various meshless or particle-based methods. The Material Point Method (MPM) [35] is a hybrid example of these, using a domain discretised into particles – 'material points' – which are used as the integration points for a background FE mesh. As shown in Fig. 1, the material points' positions are updated in each step but the mesh is discarded and reset, essentially providing a new, undistorted grid each time – regardless of the magnitude of the deformation – and minimising any adverse effects from mesh distortion. The MPM is therefore very well suited to simulating large deformation problems (e.g. [36–38]), while retaining much of the familiarity and computational simplicity of the FEM.

The MPM in its original form does however possess several minor drawbacks, including the well-known cell-crossing error, where stiffness instabilities lead to material points oscillating non-physically and exhibiting spurious stresses when moving between background grid elements. A recognised solution is adoption of the Generalised Interpolation MPM (GIMPM) [39], where material points are no longer just *points*, but exert domains of influence which may extend into several grid elements. This not only reduces oscillations, but can also help alleviate integration errors arising from poorly-filled elements. The GIMPM is therefore used later in

---

[1] Bauer et al. [29] and Grammenoudis and Tsakmakis [30] considered geometric non-linearity but made small strain assumptions.
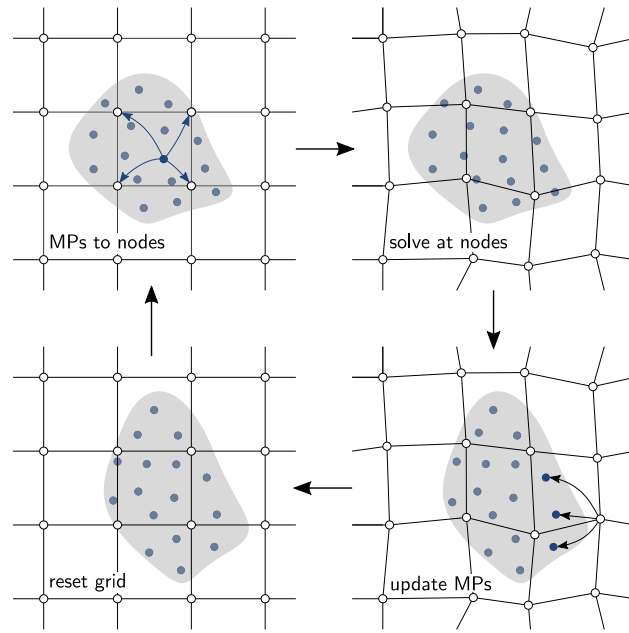
Fig. 1. The key numerical steps in the material point method.

some of the numerical examples in Section 4, and requires only minor modification to the calculation of the shape functions and their derivatives — see Charlton et al. [40] for the exact formulation used.

Following an implementation of the Particle-in-Cell method (an early, less stable precursor to the MPM) [41], a micropolar MPM first appeared only in 2022 [42]. This is an explicit method which, while very useful for highly dynamic problems, unfortunately means a well-known lack of error control, placing restrictive limits on the size of time steps. Greatly improved numerical stability is promised by instead employing implicit time integration, facilitating analyses with significantly fewer time or loadsteps[2] and reducing computational effort [43]. This is particularly the case for quasi-static problems where inertial effects are negligible.

Building on the preliminary work presented in [44], the basis of this article is therefore the development of an implicit micropolar MPM, motivated by 3D large-deformation quasi-static problems involving Hookean materials, such as those observed in the manufacture and operation of nanoscale components and assemblies. A similar approach is adopted as in [28], using the linear stress–strain laws defined in the reference/material frame. An Updated Lagrangian (UL) numerical formulation is much more suitable here, however, as a TL framework would require retention of previous reference configurations, nullifying one of the MPM's key advantages [45]. Therefore the governing equations are instead solved in the spatial frame. Microrotations are also dealt with in a careful yet numerically efficient manner, avoiding singularities encountered by other approaches (e.g. [26]) and allowing for a more concise consistent linearisation. The formulation is verified rigorously through the Method of Manufactured Solutions, demonstrating the correct numerical convergence and confirming the accuracy of the consistent tangent. Additional numerical examples are given to show that the method ably demonstrates the size effect, and can handle problems involving large rotations in three dimensions.

2. The non-linear micropolar continuum

In this section, the governing equations of non-linear micropolar theory are presented. Here, and in all that follows, lightface characters denote scalars, and those in boldface represent vectors, matrices and all tensors of order at least one. Indicial tensor notation is also used when necessary for the sake of clarity; in particular, lower-case Greek indices refer to material quantities, and lower- and upper-case Latin indices refer to spatial and numerical quantities respectively. The Einstein summation convention is employed.

2.1. Kinematics

With reference to Fig. 2, let a three-dimensional micropolar continuum occupy a volume Ω in its current (deformed) configuration. Every point in Ω exists at a Cartesian position $\boldsymbol{x}$ (relative to a fixed origin) which is referred to its initial position $\boldsymbol{X}$ in the reference volume Ω_0 via

$$\boldsymbol{x} = \boldsymbol{X} + \boldsymbol{u} \tag{1}$$

---

[2] For example, a torsion problem given in [42] used 8×10^5 time steps. A similar problem covered in Section 4.3 required only fifty.
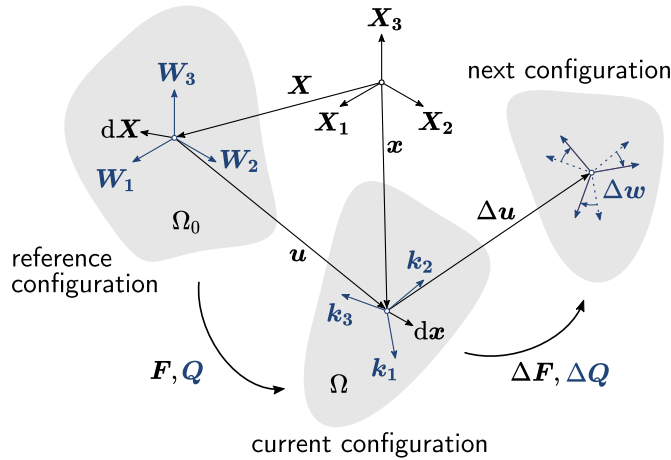
Fig. 2. The configurations of a micropolar continuum in a space described by a Cartesian coordinate system. Microrotational kinematics are shown in blue. (For interpretation of the references to colour in this figure legend, the reader is referred to the web version of this article.)

using the translation vector u. The deformation gradient tensor F provides the fundamental map $dx = F\,dX$ so that

$$F = \frac{\partial x}{\partial X} = I + \frac{\partial u}{\partial X} \tag{2}$$

where I is the second-order identity tensor, leading to a definition of local volume change $J = \det(F) > 0$ where $\det(\bullet)$ denotes the determinant.

To visualise the micropolar continuum, one may like to imagine that attached to each point in the microcontinuum is a set of three orthonormal axes.[3] These polar directors are free to rotate independently of deformation occurring at the continuum scale. The set of rotated axes $\{k_i\}_{i\in\{1,2,3\}}$ in the current configuration is related to its counterpart set $\{W_i\}$ (aligned with the Cartesian coordinate axes of the space) in the reference configuration through the relation

$$k_i = QW_i, \tag{3}$$

where, using $\otimes$ to denote the tensor product, $Q = \sum_{i=1}^{3}(k_i \otimes W_i) \in \mathrm{SO}(3)$ is a proper orthogonal transformation termed the *microrotation* tensor. The Lie group designation SO(3) (special orthogonal with three independent parameters, i.e. the 3D rotation group) means Q must fulfil certain well-known properties, namely $Q^{\mathrm{T}} = Q^{-1}$ and $\det(Q) = +1$, where $(\bullet)^{\mathrm{T}}$ denotes matrix transpose.[4] The multiplicative nature of finite rotations, exemplified by (3) (cf. the additive structure of (1)), can easily lead to confusion and thus requires careful consideration.

Via Euler's rotation theory [46], the 3D rotation transforming the reference axes into the current ones may also be parameterised as a single rotation φ occurring around some axis φ, where $\varphi = \|\varphi\|$, using $\|(\bullet)\|$ to denote the L^2-norm. This axis is known simply as the microrotation vector. The skew-symmetric tensor $\widehat{\varphi}$ for which φ is the associated axial (pseudo-)vector[5] follows as

$$\widehat{\varphi} = -e\varphi = \begin{bmatrix} 0 & -\varphi_3 & \varphi_2 \\ \varphi_3 & 0 & -\varphi_1 \\ -\varphi_2 & \varphi_1 & 0 \end{bmatrix}, \qquad \widehat{\varphi}_{ij} = -e_{ijk}\varphi_k \tag{4}$$

(where e is the third-order Levi-Civita, or *permutation*, tensor), such that $\widehat{\varphi} \in \mathfrak{so}(3)$ is a Lie algebra obeying the condition $\widehat{\varphi} = -\widehat{\varphi}^{\mathrm{T}}$. This algebra is a linearisation of the corresponding Lie group, occupying a space lying tangent to the SO(3) manifold. This tangent space can be operated in additively for plane or infinitesimal rotations, however for finite three-dimensional rotations the multiplicative microrotation tensor must be used to fully capture the field's non-linearity.

A microrotation tensor can be generated from its corresponding microrotation vector using the canonical exponential map

$$Q = \exp\left(\widehat{\varphi}\right) = \sum_{n=0}^{\infty} \frac{1}{n!}\widehat{\varphi}^n \tag{5}$$

or the (Euler-)Rodrigues formula [47]

$$Q = I + \frac{\sin\varphi}{\varphi}\widehat{\varphi} + \frac{1-\cos\varphi}{\varphi^2}\widehat{\varphi}^2 \tag{6}$$

---

[3] The *trièdre* of the Cosserat brothers [6, p. 122], sometimes translated as a *triad(e)* of *directors*.

[4] These conditions preserve the length, orthogonality and handedness of the three micropolar directors.

[5] The $\widehat{(\bullet)}$ notation is used throughout this work to indicate when a quantity is the skew-symmetric tensor formed from a vector $(\bullet)$.

in closed form. Several other methods are available for manipulation of finite rotations, including spectral decomposition and a special implementation of quaternions.[6] Note that the formal definitions (5) and (6) are not actually used in the present formulation, in favour of a quaternion rotation algorithm detailed in Section 3.2.2 utilised for its notable computational efficiency [50].

2.2. Deformation measures

The deformation gradient can now be decomposed multiplicatively[7] into a microrotation component and a stretch component

$$F = QU = VQ \tag{7}$$

where U is the material stretch tensor and V its spatial counterpart. Both stretches are generally non-symmetric. A material strain measure is then given by

$$E = U - I = Q^{\mathrm{T}}F - I. \tag{8}$$

which is also known as the 'first Cosserat deformation measure' [51]. The corresponding spatial strain measure is obtained similarly as

$$G = I - V^{-1} = I - QF^{-1} \tag{9}$$

which can be pulled back to recover

$$E = Q^{\mathrm{T}}GF. \tag{10}$$

In the micropolar continuum, a second deformation metric is required to capture the energetic contribution of changes in microrotation. Several options are available here, but in keeping with much of the literature we choose to work with the most 'natural' [52] material second-order *wryness* tensor

$$\boldsymbol{\Gamma} = -\frac{1}{2}\boldsymbol{e} : \boldsymbol{Q}^{\mathrm{T}}\frac{\partial \boldsymbol{Q}}{\partial \boldsymbol{X}}, \qquad \Gamma_{\gamma\pi} = -\frac{1}{2}e_{\gamma\tau\eta}Q_{p\tau}\frac{\partial Q_{p\eta}}{\partial X_{\pi}}, \tag{11}$$

where : denotes a double contraction. By relying on the rotation gradient, or curvature, the wryness tensor provides a sense of deformation occurring *around* the point in question, not just immediately at it. It is this quantity – the 'second Cosserat deformation measure' – which endows micropolar theory with its non-local property.

2.3. Equilibrium equations

In the quasi-static case, the balance of linear and angular momenta acting on a small (but larger in scale than that of the microstructure) spatial element of volume in Ω are given by

$$\frac{\partial \boldsymbol{\sigma}}{\partial \boldsymbol{x}} + \boldsymbol{p} = \boldsymbol{0} \tag{12}$$

$$\frac{\partial \boldsymbol{\mu}}{\partial \boldsymbol{x}} - \boldsymbol{e} : \boldsymbol{\sigma} + \boldsymbol{m} = \boldsymbol{0} \tag{13}$$

where $\boldsymbol{p}$ and $\boldsymbol{m}$ are body force and body couple loadings which lead to a Cauchy stress $\boldsymbol{\sigma}$ and couple-stress $\boldsymbol{\mu}$ field. Note that the presence of couples in the angular momentum balance equation (13), which is satisfied trivially in classical continua through equality of complementary shear stresses, means the stress tensor is not required to be symmetric in general. Eqs. (12) and (13) are coupled with Dirichlet boundary conditions which directly set the value of the primary field variables (translation and the microrotation vector) and Neumann boundary conditions

$$\boldsymbol{\sigma}\boldsymbol{n} = \bar{\boldsymbol{t}} \tag{14}$$

$$\boldsymbol{\mu}\boldsymbol{n} = \bar{\boldsymbol{t}}_{c} \tag{15}$$

where $\boldsymbol{n}$ is the outward normal vector of the surface of Ω, and $\bar{\boldsymbol{t}}$ and $\bar{\boldsymbol{t}}_{c}$ are the applied force traction and couple traction respectively.

Alternatively, by applying pull-back operations as in (10) the balance laws may be expressed in terms of material *Biot-like* stresses[8] acting on a material element of Ω_0, giving [28]

$$\frac{\partial(\boldsymbol{QB})}{\partial \boldsymbol{X}} + \boldsymbol{P} = \boldsymbol{0} \tag{16}$$

$$\frac{\partial(\boldsymbol{QS})}{\partial \boldsymbol{X}} - \boldsymbol{e} : (\boldsymbol{QBF}^{\mathrm{T}}) + \boldsymbol{M} = \boldsymbol{0} \tag{17}$$

---

[6] For a limpid and comprehensive review readers are directed to [48] and also [49] specifically for quaternions.

[7] N.B. this is not the polar decomposition conventionally performed on the deformation gradient to obtain the macrorotation $\boldsymbol{R}$. When $\boldsymbol{Q} = \boldsymbol{R}$ (i.e. when the microrotation follows the macrorotation exactly) then lower-order behaviour is recovered.

[8] Although UL formulations usually only deal with actions on the spatial body, material stresses must be considered here to permit use of the classical micropolar constitutive equations.

Table 1
The technical constants related to the constitutive parameters introduced by micropolar theory [54].

Quantity	Symbol	Physical meaning	Range	Units
Polar ratio	ψ	'Poisson's ratio for torsion'	0–1.5	–
Characteristic length in torsion	ℓ_t	Affects torsional stiffness	≥ 0	m
Characteristic length in bending	ℓ_b	Affects bending stiffness	≥ 0	m
Coupling number	N	Degree of microrotation-displacement coupling	0–1	–

where P and M are body force and couple per unit of undeformed volume. The Biot-like stress B and couple-stress S can be obtained from the Cauchy measures as follows:

$$B = J Q^{\mathrm{T}} \sigma F^{-\mathrm{T}} \tag{18}$$

$$S = J Q^{\mathrm{T}} \mu F^{-\mathrm{T}}. \tag{19}$$

2.4. Constitutive equations

The scope of this work is limited to linear materials which obey Hooke's law, so the classical micropolar constitutive laws for isotropic, centrosymmetric materials are to be employed as in Neff et al. [53]. We define them only in the reference frame to ease conservation of their objectivity. The Biot-like stresses can be obtained directly from the material strain and wryness measures as

$$B = \lambda \mathrm{tr}(E)I + \mu(1+a)E + \mu(1-a)E^{\mathrm{T}} = D : E \tag{20}$$

$$S = \alpha \mathrm{tr}(\Gamma)I + (\beta+\gamma)\Gamma + (\beta-\gamma)\Gamma^{\mathrm{T}} = \tilde{D} : \Gamma \tag{21}$$

where $\mathrm{tr}(\bullet)$ denotes matrix trace and D and $\tilde{D}$ are fourth-order constitutive tensors which include the Lamé parameters λ and μ and additional micropolar constants a, α, β and γ. Although these new constants do not necessarily have a direct physical significance, they can be related to a set of engineering parameters (described in Table 1) as follows [13]:

$$a = \frac{N^2}{1 - N^2} \tag{22}$$

$$\alpha = \frac{2\mu\ell_t^2(1-\psi)}{\psi} \tag{23}$$

$$\beta = \mu\ell_t^2 \tag{24}$$

$$\gamma = \mu(4\ell_b^2 - \ell_t^2). \tag{25}$$

Although only very limited experimental investigations have so far taken place, complete sets of these parameters have been derived for several materials including human bone and various foams [54]. It is worth remarking that couple-stress theory (also known as micropolar theory with constrained rotations) [55] may be recovered as a special case by setting the coupling number N equal to unity, and further reduction to the classical Cauchy–Boltzmann continuum is possible by assigning $a = \alpha = \beta = \gamma = 0$ [54].

3. Numerical implementation

This section does not give a complete numerical formulation as the implementation is based heavily on that of AMPLE ('A Material Point Learning Environment'), modified to accommodate the additional three rotational degrees of freedom by doubling the length of the force and solution vectors, and adapting the `detMPs.m` subroutine for the internal force, couple and stiffness calculations outlined in this section. Fields for the new rotational, stress, strain and wryness state variables at material points were also added to the structured array `mpData` to be used over the course of the analyses. Readers are referred to Coombs and Augarde [56] and the associated webpages for a more thorough exposition of the general framework used.

The continuum body Ω is divided into a number of Lagrangian material points which occupy a domain discretised into a background mesh of elements joined at nodes. Multiplying strong forms (12) and (13) by a test vectors and integrating over the volume yields corresponding weak forms, which are integrated by parts by applying the Gauss–Green theorem. The solution is approximated with trial functions which, together with the test functions, are expressed as an interpolation of nodal quantities by means of grid shape functions (which are convolved by a characteristic function in the GIMPM) contained in a matrix N, leaving the Galerkin forms of equilibrium

$$\int_{\Omega} \left(\frac{\partial N}{\partial x}\right)^{\mathrm{T}} \sigma^h \, \mathrm{d}\Omega = \int_{\Omega} N^{\mathrm{T}} p^h \, \mathrm{d}\Omega \tag{26}$$

$$\int_{\Omega} \left(\left(\frac{\partial N}{\partial x}\right)^{\mathrm{T}} \mu^h + N^{\mathrm{T}} e : \sigma^h \right) \mathrm{d}\Omega = \int_{\Omega} N^{\mathrm{T}} m^h \, \mathrm{d}\Omega. \tag{27}$$

where $(\bullet)^h$ denotes a numerical approximation. The left-hand sides represent the internal force p^{int} and couple m^{int} vectors while the right-hand sides represent the external loadings p^{ext} and m^{ext}.

3.1. Solution procedure

Solution of the discretised boundary-value problem for a fixed external load with a Newton–Raphson scheme requires an iterative sequence of consistent linearisation and incrementation of the LHSs of (26) and (27) until a convergence criterion is met. The linearisation procedure produces a tangent stiffness matrix $\boldsymbol{K}$ which essentially relates an increment in deformation to an increment in force and couple, such that

$$\Delta p^{\text{int}} = \boldsymbol{K}^{pu} \Delta \boldsymbol{u} + \boldsymbol{K}^{pw} \Delta \boldsymbol{w} \tag{28}$$

$$\Delta m^{\text{int}} = \boldsymbol{K}^{mu} \Delta \boldsymbol{u} + \boldsymbol{K}^{mw} \Delta \boldsymbol{w} \tag{29}$$

where $\Delta \boldsymbol{w}$ denotes an incremental rotation relative to the follower axes $\boldsymbol{k}$ as oriented at the beginning of the current iteration. The four submatrices which comprise the tangent stiffness matrix are derived fully in Appendix A, but for a single element E they read

$$\boldsymbol{K}_E^{pu} = \int_E \boldsymbol{G}^{\mathrm{T}} : \mathbf{a} : \boldsymbol{G} \, d\Omega \tag{30}$$

$$\boldsymbol{K}_E^{pw} = \int_E \boldsymbol{G}^{\mathrm{T}} : \mathbf{b} : \tilde{\boldsymbol{G}} \, d\Omega \tag{31}$$

$$\boldsymbol{K}_E^{qu} = \int_E \tilde{\boldsymbol{G}}^{\mathrm{T}} : \mathbf{b}^{\mathrm{T}} : \boldsymbol{G} \, d\Omega \tag{32}$$

$$\boldsymbol{K}_E^{qw} = \int_E \left(\tilde{\boldsymbol{G}}^{\mathrm{T}} : \mathbf{b} : \tilde{\boldsymbol{G}} + \boldsymbol{G}^{\mathrm{T}} : \left(\mathbf{c} : \boldsymbol{G} + \mathbf{d} : \tilde{\boldsymbol{G}} \right) \right) d\Omega \tag{33}$$

where

$$\mathbf{a} = J^{-1} \boldsymbol{T} : \boldsymbol{D} : \boldsymbol{T}^{\mathrm{T}} \tag{34}$$

$$\mathbf{b} = \mathbf{a} + \boldsymbol{\Sigma} \tag{35}$$

$$\mathbf{c} = J^{-1} \boldsymbol{T} : \tilde{\boldsymbol{D}} : \boldsymbol{T}^{\mathrm{T}} \tag{36}$$

and for which it is more convenient to use index notation to define

$$T_{ij\alpha\beta} = Q_{i\alpha} F_{j\beta} \tag{37}$$

$$\Sigma_{ijkl} = \delta_{il}\sigma_{kj} \tag{38}$$

$$d_{ijkl} = \delta_{il}\mu_{kj} \tag{39}$$

in which δ_{ij} is the Kronecker delta. The matrices $\boldsymbol{G}$ and $\tilde{\boldsymbol{G}}$ contain the shape functions or their spatial derivatives in the forms

$$\boldsymbol{G} = \begin{bmatrix}
\frac{\partial N_1}{\partial x} & 0 & 0 & \cdots & \frac{\partial N_{n_n}}{\partial x} & 0 & 0 \\
0 & \frac{\partial N_1}{\partial y} & 0 & \cdots & 0 & \frac{\partial N_{n_n}}{\partial y} & 0 \\
0 & 0 & \frac{\partial N_1}{\partial z} & \cdots & 0 & 0 & \frac{\partial N_{n_n}}{\partial z} \\
\frac{\partial N_1}{\partial y} & 0 & 0 & \cdots & \frac{\partial N_{n_n}}{\partial y} & 0 & 0 \\
0 & \frac{\partial N_1}{\partial x} & 0 & \cdots & 0 & \frac{\partial N_{n_n}}{\partial x} & 0 \\
0 & \frac{\partial N_1}{\partial z} & 0 & \cdots & 0 & \frac{\partial N_{n_n}}{\partial z} & 0 \\
0 & 0 & \frac{\partial N_1}{\partial y} & \cdots & 0 & 0 & \frac{\partial N_{n_n}}{\partial y} \\
0 & 0 & \frac{\partial N_1}{\partial x} & \cdots & 0 & 0 & \frac{\partial N_{n_n}}{\partial x} \\
\frac{\partial N_1}{\partial z} & 0 & 0 & \cdots & \frac{\partial N_{n_n}}{\partial z} & 0 & 0
\end{bmatrix} \tag{40}$$

$$\tilde{\boldsymbol{G}} = \begin{bmatrix}
0 & 0 & 0 & \cdots & 0 & 0 & 0 \\
0 & 0 & 0 & \cdots & 0 & 0 & 0 \\
0 & 0 & 0 & \cdots & 0 & 0 & 0 \\
0 & 0 & N_1 & \cdots & 0 & 0 & N_{n_n} \\
0 & 0 & -N_1 & \cdots & 0 & 0 & -N_{n_n} \\
0 & N_1 & 0 & \cdots & 0 & N_{n_n} & 0 \\
0 & -N_1 & 0 & \cdots & 0 & -N_{n_n} & 0 \\
N_1 & 0 & 0 & \cdots & N_{n_n} & 0 & 0 \\
-N_1 & 0 & 0 & \cdots & -N_{n_n} & 0 & 0
\end{bmatrix}, \tag{41}$$

where n_n is the number of nodes affected by a material point, which is simply the number of nodes per element in the standard MPM.

The submatrices are assembled DOF-wise to make the global set of equations

$$\begin{Bmatrix} \boldsymbol{p}^{\text{res}} \\ \boldsymbol{m}^{\text{res}} \end{Bmatrix} = \begin{bmatrix} \boldsymbol{K}^{pu} & \boldsymbol{K}^{pw} \\ \boldsymbol{K}^{mu} & \boldsymbol{K}^{mw} \end{bmatrix} \begin{Bmatrix} \Delta \boldsymbol{u} \\ \Delta \boldsymbol{w} \end{Bmatrix}. \tag{42}$$

This system is solved iteratively by taking the solution vector $\left\{ \begin{smallmatrix} \Delta u \\ \Delta w \end{smallmatrix} \right\}$ each time, updating the kinematics and stress fields accordingly, and checking whether the residual force $\boldsymbol{p}^{\text{res}}$ and couple $\boldsymbol{m}^{\text{res}}$, where $(\bullet)^{\text{res}} = (\bullet)^{\text{ext}} - (\bullet)^{\text{int}}$, are smaller than some degree of tolerance — typically of the order 10^{-9} when normalised by the external load.

3.2. Update procedure

This section details the mapping of field variables from the nodes to, and the update of history variables at, the material points. Quantities described at grid nodes and material points are denoted with $(\bullet)_H$ and $(\bullet)_P$ respectively and, as a reminder, $\widehat{(\bullet)}$ denotes the skew-symmetric tensor formed from the components of a vector $(\bullet)$ — see (4).

3.2.1. Translation
The incremental translations $\Delta \boldsymbol{u}_H$ are extracted from the solution vector and mapped to each material point via the shape functions, i.e.

$$\Delta \boldsymbol{u}_P = \boldsymbol{N} \Delta \boldsymbol{u}_H. \tag{43}$$

The material point's position is then simple to update using the additive formula

$$\boldsymbol{x}_P^{N+1} = \boldsymbol{x}_P^N + \Delta \boldsymbol{u}_P. \tag{44}$$

3.2.2. Rotation
There is no perfect way to interpolate rotation parameters using conventional Lagrange polynomial interpolants [57]. This is for a number of reasons. For example, interpolating the nine individual values of the rotation tensor itself would erode its properties, no longer guaranteeing a proper orthogonal rigid motion. A common alternative is to instead interpolate the equivalent rotation vector; while this *does* ensure a rotation tensor fully adhering to the SO(3) conditions, its spatial variation unfortunately cannot be fully captured by an isoparametric interpolation procedure based on additive contributions. This is because rotation vectors do not belong on a linear manifold or plane, and thus their concatenation cannot be achieved by simple addition. Instead they exist in curvilinear space — a sphere of radius π (or 2π, depending on the definition used) [48]. More rigorous methods for rotation interpolation do exist, such as Spherical Linear intERPolation (SLERP) [49], but these inevitably come with added computational cost, and generalisations beyond one-dimensional interpolation are crude (if they even exist at all). A non-standard interpolation of the solution field would also have severe implications for the complexity of the consistent tangent and the method in general. Therefore, despite the method's faults, the chosen approach is to use a conventional Lagrange polynomial interpolation of the microrotation vector in the same way that the translation vector is interpolated above, i.e.

$$\Delta \boldsymbol{w}_P = \boldsymbol{N} \Delta \boldsymbol{w}_H. \tag{45}$$

This means, however, that over the course of several iterations the poor interpolation is iteratively embedded into the value of the microrotation tensor, leading to path dependency as first noted by Jelenić and Crisfield [58].[9] But because imperfectly filled elements engender integration errors (which depend on the path taken by the body through the grid) in the MPM anyway, the additional path dependency invoked by non-rigorous rotation interpolation is unlikely to diminish the reliability of the method by any significant degree. Therefore, although we acknowledge this flaw (which in the literature is usually ignored), we consider it too minor to merit further consideration here and leave it as an open problem outside the scope of this contribution.

Clear distinction must now be drawn between the material 'total' rotation $\boldsymbol{\varphi}$, which is measured relative to the reference axes $\boldsymbol{W}_i$, and the spatial 'spin' rotation $\boldsymbol{w}$, which occurs relative to the rotating follower axes $\boldsymbol{k}_i$. It is an increment in the latter for which the numerical algorithm solves in each iteration and is mapped to the material points. Crucially, however, one must recognise that a new total rotation *cannot* be updated directly using this increment, i.e.

$$\boldsymbol{\varphi}^{N+1} \neq \boldsymbol{\varphi}^N + \Delta \boldsymbol{w}, \tag{46}$$

and instead a multiplicative update procedure must be used as follows.[10] The new rotation tensor is updated from its existing value using the increment $\Delta \boldsymbol{Q} = \exp\left\{ \widehat{(\Delta \boldsymbol{w}_P)} \right\}$ given by the exponential mapping (5) or equivalent, as

$$\boldsymbol{Q}^{N+1} = (\Delta \boldsymbol{Q}) \boldsymbol{Q}^N. \tag{47}$$

---

[9] See Sansour and Wagner [57] for a solution to this problem if this work is to be repurposed for a conventional Lagrangian FEM. It cannot unfortunately be applied to the MPM as the proposed method requires storing history variables at grid nodes.

[10] It is possible to formulate an approach which deals only with the total rotation vector $\boldsymbol{\varphi}$ and linear increments thereof (as done in [26]), but this leads to an (even) more demanding linearisation and a cumbersome consistent tangent involving expensive evaluation of trigonometric functions. The rotation vector formalism, when used alone in this way, also suffers from singularities due to loss of axis direction when passing through whole revolutions [50].

Updating the rotation tensor in this way, however, is known to be computationally expensive, and can invoke poor conditioning at $\varphi \approx n\pi, \forall\, n \in \mathbb{Z}$. The preferred method is via quaternions which, despite being less intuitive than rotation matrices, are a demonstrably more efficient and robust way to represent and manipulate elements of SO(3) [49,50]. Moreover, by depending on more than three independent parameters, the quaternion formalism does not suffer from a singularity known as *gimbal lock*[11] experienced by some other representations of unrestrained rotation.

A quaternion $\mathcal{Q}$ consists of a real scalar component q and an imaginary vector component $\boldsymbol{q}$ such that $\mathcal{Q} = q + i\boldsymbol{q}$, where i is the imaginary unit. The reference form of $\mathcal{Q}$, corresponding to the identity rotation tensor $\boldsymbol{Q} = \boldsymbol{I}$ (i.e. when there are no rotations), is

$$Q^0 = 1 + i \left\{ \begin{matrix} 0 \\ 0 \\ 0 \end{matrix} \right\} \tag{48}$$

and the quaternion increment is

$$\Delta Q = \Delta q + i\Delta\boldsymbol{q} = \cos\left(\frac{\Delta w}{2}\right) + i\left(\frac{\sin\left(\frac{\Delta w}{2}\right)}{\Delta w}\Delta\boldsymbol{w}\right) \tag{49}$$

where $\Delta w = \|\Delta\boldsymbol{w}\|$, using the formulae of Erdelj et al. [28] based on the work of Ibrahimbegović and co-workers [59,60]. Using · and × to denote respectively the dot and cross products, the updated quaternion is computed via the increment as

$$Q^{N+1} = \left(q^N \Delta q - \boldsymbol{q}^N \cdot \Delta\boldsymbol{q}\right) + i\left(\Delta\boldsymbol{q} \times \boldsymbol{q}^N + q^N \Delta\boldsymbol{q} + \Delta q\boldsymbol{q}^N\right) \tag{50}$$

$$= q^{N+1} + i\boldsymbol{q}^{N+1}. \tag{51}$$

Finally, the corresponding rotation tensor can be generated from a quaternion via

$$\boldsymbol{Q} = (2q^2 - 1)\boldsymbol{I} + 2q\widehat{\boldsymbol{q}} + 2\boldsymbol{q} \otimes \boldsymbol{q}. \tag{52}$$

Although not strictly required for the formulation, producing the corresponding microrotation vector $\boldsymbol{\varphi}$ as an output can provide for a less abstract reification of the deformation than the microrotation tensor *per se*. There are several ways to achieve this. For example, taking the matrix logarithm of $\boldsymbol{Q}$ gives the skew-symmetric tensor $\widehat{\boldsymbol{\varphi}}$ for which $\boldsymbol{\varphi}$ is the axial vector. However, this is an expensive computation to perform and, due to the periodicity of rotations, can only return $-\pi < \varphi \leq \pi$. Instead, the microrotation vector may be obtained directly from the quaternion as

$$\boldsymbol{\varphi} = \frac{2\arccos(q)}{\sqrt{1 - q^2}}\boldsymbol{q} \tag{53}$$

which, although still not bijective, has the added benefit of widening the interval to $-2\pi < \varphi \leq 2\pi$.

3.2.3. Deformation gradient

The deformation gradient tensor is updated as in the usual formulation of AMPLE [56] after the work of Charlton et al. [40]. In brief,

$$\boldsymbol{F}^{N+1} = (\Delta\boldsymbol{F})\boldsymbol{F}^N \tag{54}$$

where $\Delta\boldsymbol{F}$ is the incremental deformation gradient linking the last state to the current state.

3.2.4. Wryness

The map $\boldsymbol{H}$ which relates a spin rotation vector increment $\Delta\boldsymbol{w}$ to its equivalent linear material increment $\Delta\boldsymbol{\varphi}$ such that $\Delta\boldsymbol{w} = \boldsymbol{H}^{\mathrm{T}}\Delta\boldsymbol{\varphi}$ (see e.g. [58]) is defined

$$\boldsymbol{H} = \boldsymbol{I} + \frac{1 - \cos(\Delta w)}{(\Delta w)^2}\widehat{\Delta\boldsymbol{w}} + \frac{\Delta w - \sin(\Delta w)}{(\Delta w)^3}\widehat{\Delta\boldsymbol{w}}^2. \tag{55}$$

The wryness tensor is then updated with the formula of Erdelj et al. [28],

$$\boldsymbol{\Gamma}^{N+1} = \boldsymbol{\Gamma}^N + \boldsymbol{Q}^{\mathrm{T}}\boldsymbol{H}\frac{\partial(\Delta\boldsymbol{w})}{\partial\boldsymbol{x}}\boldsymbol{F} \tag{56}$$

for which the spatial gradient of the rotation vector increment is produced using the derivatives of the shape functions.

The material point stress update algorithm is given in Algorithm 1.

4. Numerical examples

In all the following examples, the Newton–Raphson algorithm is halted when two criteria are met: when the force residual is less than 10^{-9} and the energy residual is less than 10^{-16}. The force residual is computed by taking the Euclidean norm of the force/couple residual vector and dividing by the norm of the external load vector, and the energy residual is the inner product of the force/couple residual vector and the incremental deformations (the solution vector).

---

[11] N.B. this is distinct from the other type of singularity mentioned elsewhere in this section.

Algorithm 1 Procedure for updating stress and couple-stress at the material points in iteration $N + 1$.

1: Node-to-MP mapping.

1a: Extract translation and microrotation vector increments from the solution vector.

1b: Map to material points using standard or GIMPM shape functions and their derivatives computed in the previous iteration to obtain $\Delta \boldsymbol{u}_P$, $\Delta \boldsymbol{w}_P$, $\frac{\partial (\Delta \boldsymbol{u}_P)}{\partial \boldsymbol{x}^N}$ and $\frac{\partial (\Delta \boldsymbol{w}_P)}{\partial \boldsymbol{x}^N}$.

2: Kinematic update procedure.

2a: Update deformation gradient:

$$\boldsymbol{F}^{N+1} = (\Delta \boldsymbol{F}) \boldsymbol{F}^N = \left(\boldsymbol{I} + \frac{\partial (\Delta \boldsymbol{u})}{\partial \boldsymbol{x}^N} \right) \boldsymbol{F}^N.$$

2b: Update derivatives:

$$\frac{\partial (\bullet)}{\partial \boldsymbol{x}^{N+1}} = \frac{\partial (\bullet)}{\partial \boldsymbol{x}^N} (\Delta \boldsymbol{F})^{-1}.$$

2c: Update quaternion using (49)–(51) and calculate the microrotation tensor with (52).

2d (optional): Compute the corresponding microrotation vector with (53).

3: Stress update procedure.

3a: Calculate material strain and wryness with (8) and (55)–(56) respectively.

3b: Obtain material Biot-like stress and couple-stress with constitutive laws (20) and (21).

3c: Push forward for spatial Cauchy stress and couple-stress:

$$\boldsymbol{\sigma} = J^{-1} \boldsymbol{Q} \boldsymbol{B} \boldsymbol{F}^{\mathrm{T}} \quad \text{and} \quad \boldsymbol{\mu} = J^{-1} \boldsymbol{Q} \boldsymbol{S} \boldsymbol{F}^{\mathrm{T}}.$$

4.1. Method of manufactured solutions

In the absence of many[12] existing analytic benchmark problems for non-linear micropolar theory, the formulation's accuracy and convergence properties are assessed by means of the Method of Manufactured Solutions (MMS). In the MMS for solid mechanics, a synthetic solution field is designed and the corresponding body force/couple and boundary conditions are generated via the full nonlinear kinematic framework and governing equations.[13] Numerical accuracy is then observed by comparing the numerically-approximated solution of the problem with the manufactured analytical solution. To that end, the arbitrary displacement-rotation field

$$u_1 = \cdots = \varphi_3 = A \sin \left(2\pi X_1 \right) \sin \left(2\pi X_2 \right) \sin \left(2\pi X_3 \right), \tag{57}$$

was chosen, where $X_i \in [0, 1]$ defines a unit cube domain and $A = \frac{1}{30}$ ensures that displacement is sufficiently small to guarantee numerical stability. This particular trigonometric function was constructed as it is continuously and infinitely differentiable and cannot be captured exactly by polynomial interpolation. The boundary conditions consistent with (57) require fixing all translation and microrotation components at nil over all six sides of the domain.

In this study, the problem is simulated with a mesh discretisation of tri-linear hexahedral elements and 2^3 material points per element located at their Gauss–Legendre placements. The conventional MPM is used (as opposed to the GIMPM) and the loads are applied in a single loadstep. This effectively transforms the scheme into a finite element analysis, with the purpose of eliminating the integration errors associated with the MPM to allow for clearer assessment of the coercivity of the core parts of the method. Although the chosen constitutive parameters really have no relevance to the problem (as long as they are thermodynamically consistent), the values used are: $\lambda = 15$ GPa, $\mu = 10$ GPa, $a = \frac{1}{3}$, $\alpha = 0$ N, $\beta = \gamma = 50$ N. The displacement/rotation error e_d and Cauchy stress error e_s are computed using

$$e_d = \int_\Omega \| (\boldsymbol{d}^h - \boldsymbol{d}^a) \| \, \mathrm{d}\Omega \tag{58}$$

$$e_s = \int_\Omega \frac{\| (\boldsymbol{s}^h - \boldsymbol{s}^a) \|}{\| \boldsymbol{s}^a \|} \, \mathrm{d}\Omega \tag{59}$$

where $(\bullet)^h$ and $(\bullet)^a$ are the numerical and analytical solutions, and $\boldsymbol{d}$ and $\boldsymbol{s}$ are the translation/rotation vector and stress tensors, respectively. The resulting convergence graphs for elements of decreasing dimension h are shown on log–log scales in Figs. 3(a) and

---

[12] The analytical solution describing the response of a geometrically-nonlinear micropolar cantilever is given in [28,61], but as it would require application of a non-conforming Neumann boundary condition (which is non-trivial in the MPM [62]), we have chosen to derive a novel benchmark problem to avoid unnecessary complication of the derived method solely for the purpose of its own validation.

[13] Expressions for the requisite body force and couple were produced using MATLAB's Symbolic Math Toolbox™. Realistically their sheer length precludes them from being listed here.
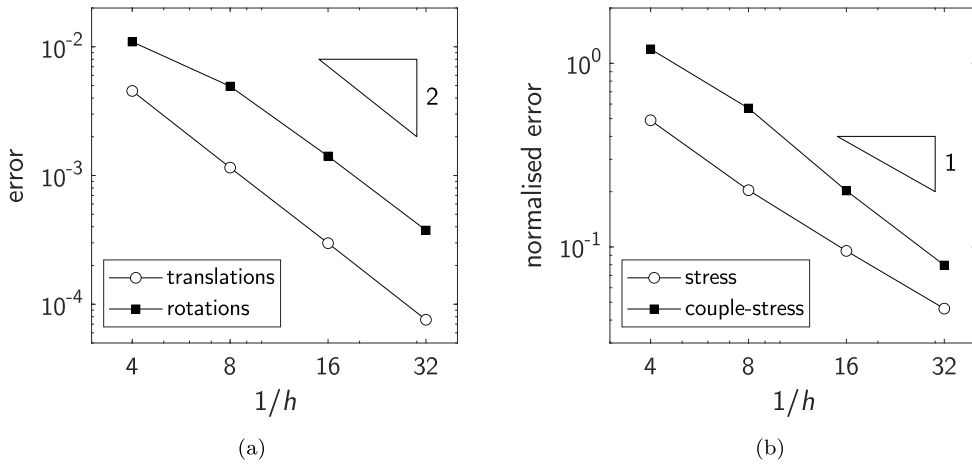
Fig. 3. Convergence with mesh refinement of (a) translations and rotations and (b) Cauchy stress and couple-stress.
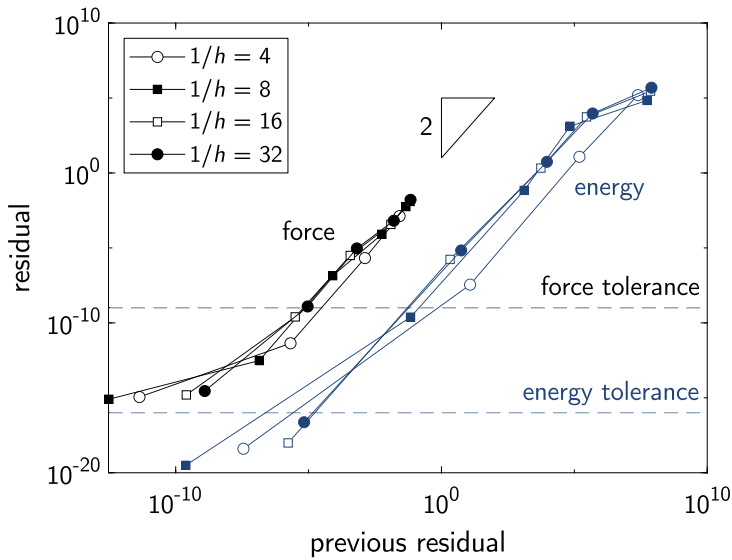
Fig. 4. Newton–Raphson convergence of the energy and normalised force residuals.

3(b). As linear elements are used, quadratic displacement and (approaching) linear stress error decay is observed, showing that the results are consistent with the governing equations. In other words, the method solves the partial differential equations in accordance with the non-linear framework proposed in Section 2. It is postulated that the relatively poorer convergence of the rotation and couple-stress is a direct consequence of the poor quality of the rotation interpolation used in the method. This issue is known to diminish on finer meshes [58], as indicated by the supralinear convergence of the couple-stress errors towards the stress errors. Fig. 4 shows the progression of the normalised force and energy residuals in each of the analyses, demonstrating asymptotically quadratic convergence (until being hampered by machine precision). It is well known that, when implemented fully and correctly, the Newton–Raphson algorithm delivers this rate of asymptotic convergence in the region of the solution [63]. Crucially, therefore, this endorses the consistency of the derived tangent.

4.2. Cantilever beam under bending

This and the following torsion example make use of a 3D GIMPM implementation with a regular hexahedral background mesh of tri-linear elements occupied by material points which are equally spaced in each direction.

As shown in Fig. 5, an ($L_0 = 10$ m) × 1 m × 1 m beam in plane strain (i.e. with all out-of-plane deformations constrained) is subject to an end load of 50 kN applied in 50 equal loadsteps; $\lambda = 3.333$ MPa, $\mu = 5$ MPa, $a = \frac{1}{3}$, $\alpha = 0$ N and $\beta = \gamma =$ (a) 100 kN or
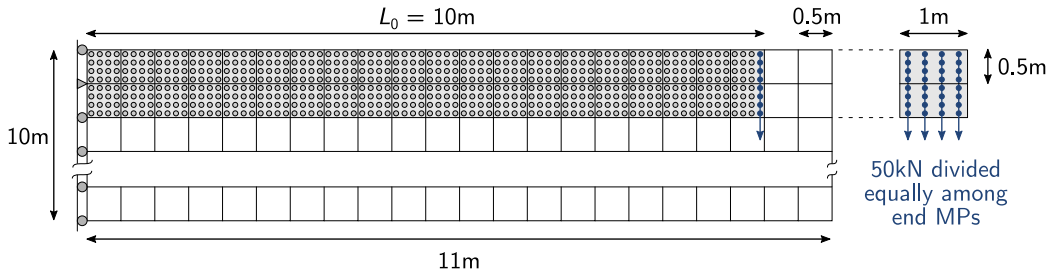
Fig. 5. Setup of the cantilever beam problem.

(a) $L_0 = 100\ell_b$ (b) $L_0 = 10\ell_b$
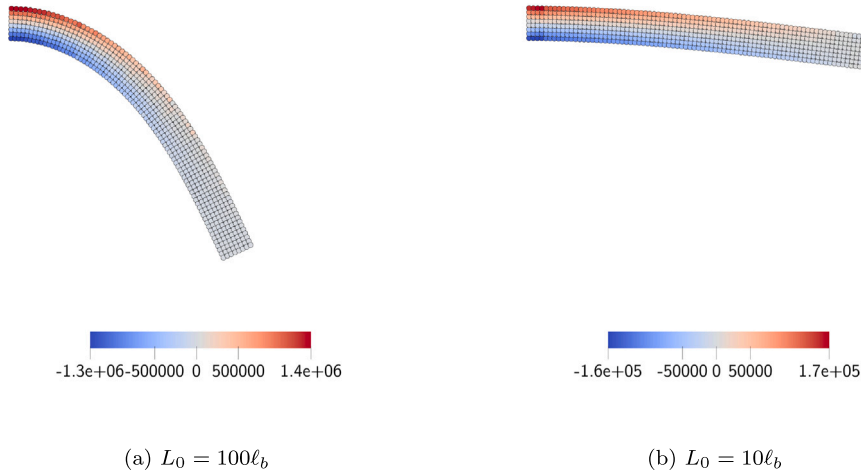
Fig. 6. Bending of two cantilever beams with different microstructural scales, coloured according to horizontal normal stress. (For interpretation of the references to colour in this figure legend, the reader is referred to the web version of this article.)

(b) 10 MN. The bending characteristic lengths ℓ_b = (a) 0.1 m and (b) 1 m are calculated using

$$\ell_b = \sqrt{\frac{\beta + \gamma}{4\mu}}. \tag{60}$$

The grid elements are 0.5 m × 0.5 m × 1 m in size and are occupied by 4^3 material points each. The increased number of material points is to minimise integration errors from poorly filled elements as the body progresses through the mesh. Roller boundaries are applied at the root of the beam, allowing movement vertically but fixing the beam horizontally, and a pin at the beam's mid-point restricts motion both vertically and horizontally. All rotations are additionally fixed equal to zero along the root. The load is applied as a set of point forces divided equally among the plane of material points nearest to the tip of the beam, forming a 'pseudo-Neumann' boundary condition.

This example essentially demonstrates the size effect in two microscopically small beams whose overall structural scales are comparable to those of their constituent microstructures. This genre of problem has received particular interest recently due to its relevance to microelectromechanical systems (MEMS) and other nanoscale industrial applications. As shown by experimental results (see e.g. [1,64,65]), the microstructure has a greater influence when it is closer in scale to the size of the overall structure, manifesting as a substantial stiffening and/or hardening via the Hall–Petch mechanism or similar [2]. This is reflected in the numerical results depicted in Figs. 6 and 7, which show a much stiffer response and smaller final displacement for the beam with the larger characteristic length. The apparent stiffening towards the end of the analysis in case (a) is due to the principal mode of deformation transitioning from bending to axial tension.

4.3. Cantilever shaft under torsion

With reference to Fig. 8, a 5 m × 1 m × 1 m shaft is subject to an end moment of 8×10^6 kN m applied in 50 equal loadsteps; grid elements are 0.25 m × 0.25 m × 0.25 m and are occupied by 2^3 material points each, $\lambda = 3.333$ MPa, $\mu = 5$ MPa, $a = \frac{1}{3}$, $\alpha = 0$ N and $\beta = \gamma = 10$ MN. The corresponding torsion characteristic length is $\ell_t = \sqrt{2}$ m, via

$$\ell_t = \sqrt{\frac{\beta}{\mu}}. \tag{61}$$
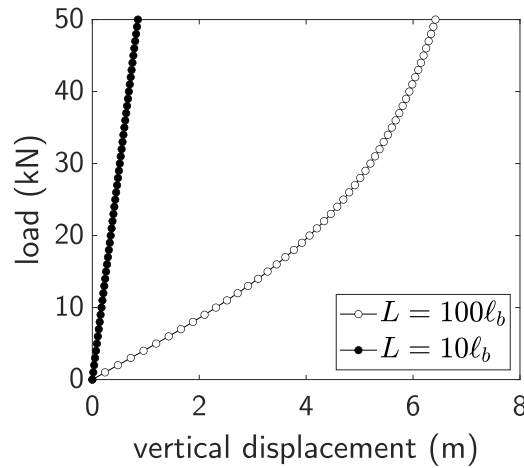
Fig. 7. The load–displacement response of the two beams. The vertical displacement shown is that of the bottom-most material points at the tip of the beam.
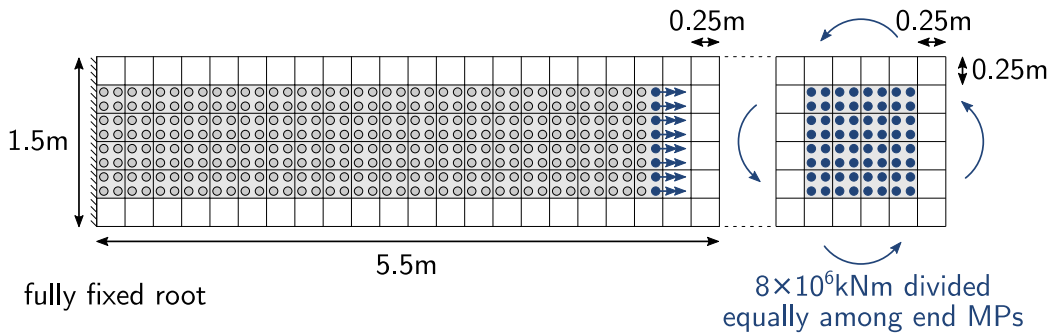
Fig. 8. Setup of the cantilever shaft problem. The double arrowheads use a right hand rule to denote an applied couple.

The entire boundary at the root of the shaft is fully fixed, in terms of both translations and rotations. As with the cantilever problem, the end moment is applied by dividing the total amount equally among the final 64 material points which are closest to the shaft's tip.

This problem was designed to verify that the method can handle rotations in excess of 2π radians without being affected either by gimbal lock or the singularity associated with the rotation vector formalism. As shown in Fig. 9, the angle of twist does not reach an artificial cap at 2π, but is able to push through this limit on the formal definition of the rotation vector. The displacement solution remains smooth through the transition (represented by the jump in colour in Fig. 9(f) due to the periodic nature of (53)) without ill conditioning of the system as might otherwise be expected. This demonstrates that the method is robust even for very large rotations.

The rotation vector singularity does in fact appear in Fig. 9(f), however. At a complete revolution the axis of rotation becomes indeterminate, resulting in some of the material points at the transition showing spurious axial rotation values where the expected result is $\varphi_x \approx \pm 2\pi$. The large divergence of this representation from the actual physical behaviour here would introduce significant errors into any method which directly uses the rotation vector formalism in its formulation. However, any errors or ill conditioning that might be produced as a result of this singularity are completely avoided by our method. The rotation vector is only computed as an output for graphical purposes and is not used in the internal force/couple calculations or kinematic update algorithm.

4.4. 45° curved cantilever

Although the examples presented in the previous sections involve large rotations, in both cases the axis of rotation remains fixed throughout the analysis. This degenerates the rotation parameters to a single scalar (the rotation angle) which could be captured by a simple linearised version of the formulation. Therefore, to validate the geometrically-exact rotation machinery described in Section 3, the method must be tested with a problem involving large, genuinely three-dimensional rotations, i.e. one with a varying axis of rotation. Accordingly, the 45° curved cantilever of Bathe and Bolourchi [66] was selected, which was originally designed as a benchmark problem for beam analysis, but was repurposed by Erdelj et al. [28] for the nonlinear micropolar continuum. As depicted in Fig. 10, a circular arc of radius 100 m subtending an angle of 45° at its centre (i.e. forming one eighth of a circle) with

(a) initial configuration

(b) loadstep 10

(c) loadstep 20

(d) loadstep 30

(e) loadstep 40

(f) loadstep 50 (final configuration)
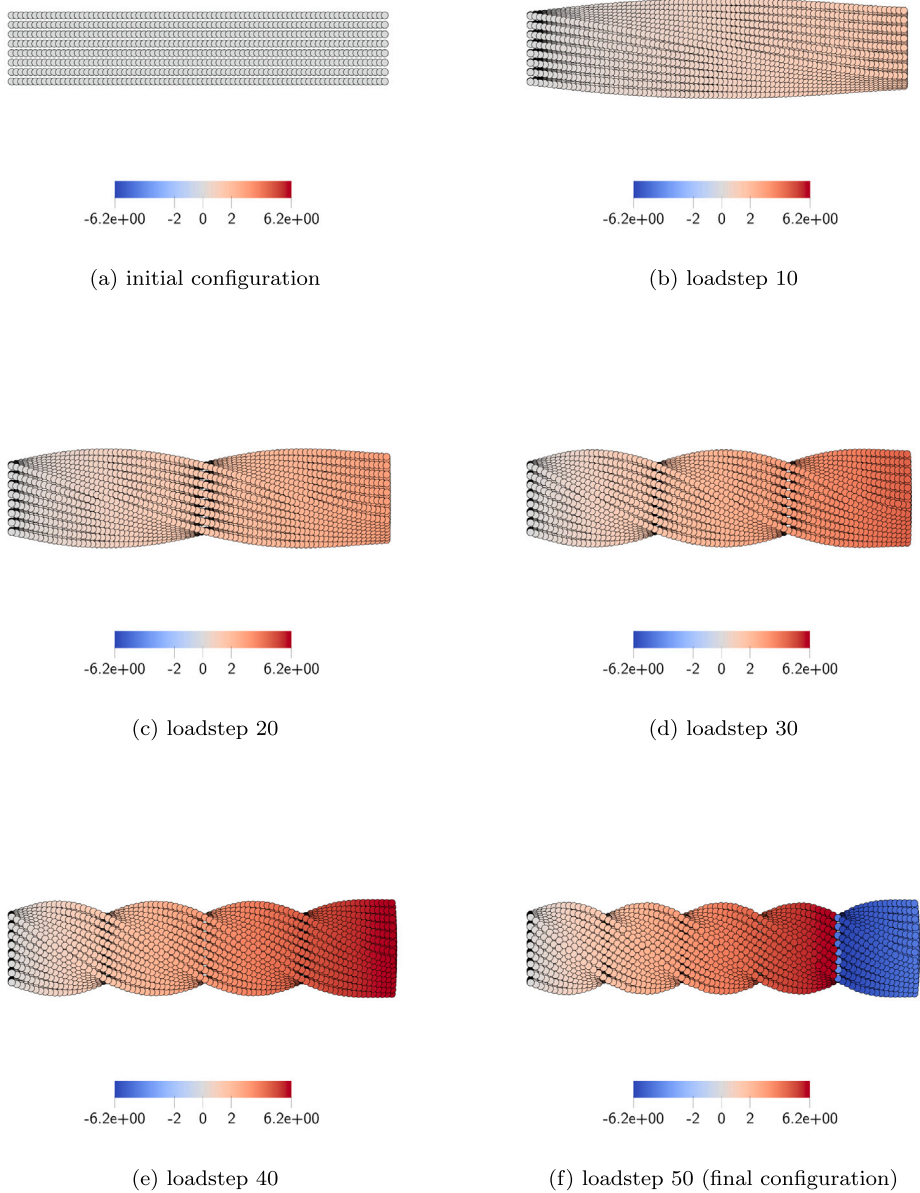
Fig. 9. The cantilever shaft under torsion, coloured according to the component of the microrotation vector showing the angle of rotation around the shaft's longitudinal axis (the x-axis).

a 1 m × 1 m square cross-section is loaded in 15 equal loadsteps with an end load of 600 N pulling in an out-of-plane direction. The other end of the cantilever is fully fixed in both translation and rotation. As for the material parameters, these are kept the same as in [28] in order to allow for a more valid comparison with the analytical result of [67]: $\lambda = 0$ Pa, $\mu = 5$ MPa, $a = \frac{50505.1}{5\times10^6}$, $\alpha = 0$, $\beta = 12500$ and $\gamma = 37500$, corresponding to $N = 0.1$, $\ell_b = \ell_t = 0.05$m and $\psi = 1$, as well as a Young's modulus of 10 MPa and a Poisson's ratio of 0. However, as the analytical solution in [67] assumes a classical, albeit geometrically-exact, mechanical formulation, exact convergence will never be observed and the micropolar response will always differ slightly due to size effects, regardless of a careful selection of parameters.

Additionally, for the purpose of comparison, this example was also tested in a FEM developed from the same framework described above for the MPM — essentially a UL version of the method presented in [28]. Unfortunately, as shown in Fig. 11 a direct comparison between the two methods is impossible due to significant differences in discretisation procedures: in the FEM, the arch is discretised into a number of hexahedrons by subdividing it in the circumferential, radial and out-of-plane directions; in the MPM, the entire domain is seeded with material points, and any which lie outside the extremities of the arch are discarded. Moreover, the end loading is achieved in the FEM by integrating an equivalent constant traction of 600 Pa over the end surface of the arch; in
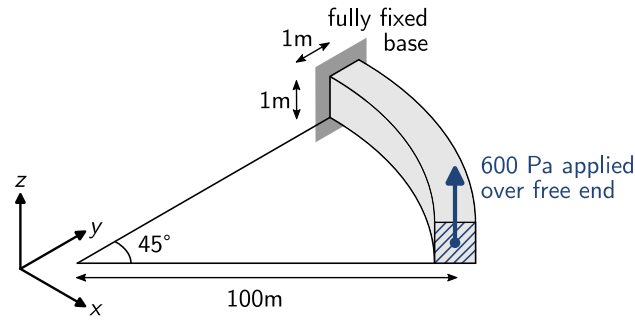
Fig. 10. Setup of the 45° curved cantilever.
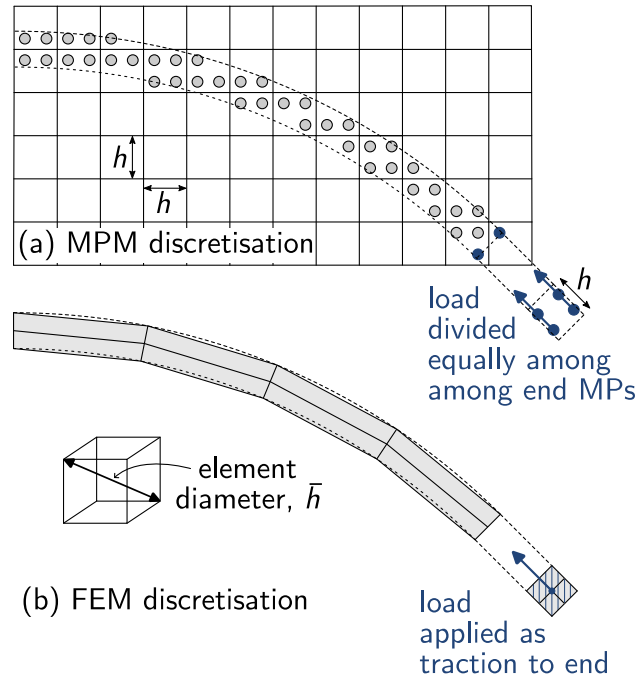
Fig. 11. Illustrative discretisations of the 45° curved cantilever; neither discretisation shown is actually used in the analysis. In the MPM example (a), the background grid is composed of elements of dimensions h^3 filled with 2^3 material points each. In the FEM example (b), the arch is discretised into a mesh of $4 \times 2 \times 2$ elements. Comparison of mesh size is possible by determining the element diameter $\bar{h}$ for each case as shown.

Table 2
Results obtained using the FEM with trilinear hexahedral elements. The displacements are calculated by averaging the nodal solution over the end of the cantilever.

No. elements	u_x	u_y	u_z	e_d	$\bar{h}$	CPU time (s)
$64 \times 1 \times 1$	−14.40	8.52	43.40	14.21	1.87	7.9
$128 \times 2 \times 2$	−20.04	11.64	50.05	4.96	0.94	153.8
$256 \times 4 \times 4$	−22.18	12.83	52.14	1.75	0.47	5425.0
Analytical soln. [67]	−23.30	13.64	53.21	–	–	–

the MPM the load is applied as a set of point forces on the plane of material points closest to the free end of the cantilever, as with the previous examples. A crude comparison between the methods is made by measuring the diameter $\bar{h}$ of either the finite element or the MPM grid cell: the longest vertex-to-vertex distance, which is equivalently the diameter of the sphere circumscribed about the element. This allows for observation of the two methods' relative performance in terms of h-convergence towards the analytical solution as well as the incurred computational cost, as given in Tables 2 and 3, where the displacement error e_d is calculated with (58). The MPM example with the finest mesh is also depicted in Fig. 12, showing both the initial and final states of the cantilever.

Although a convergence order of between one and two is observed for both methods (see Fig. 13), the MPM implementation produces an end displacement roughly an order of magnitude closer to the analytical solution for a comparable element size. This

Table 3

Results obtained using the MPM with 4^3 MPs per grid cell. The displacements are calculating by averaging the solution across the end MPs (the same MPs to which the load was applied).

Grid cell dims. (m)	u_x	u_y	u_z	e_d	$\bar{h}$	CPU time (s)
$2 \times 2 \times 2$	−22.00	16.57	48.10	6.03	3.46	90.1
$1 \times 1 \times 1$	−23.52	14.27	52.08	1.31	1.73	792.7
$0.5 \times 0.5 \times 0.5$	−23.67	13.74	53.09	0.40	0.87	23 736.5
Analytical soln. [67]	−23.30	13.64	53.21	–	–	–
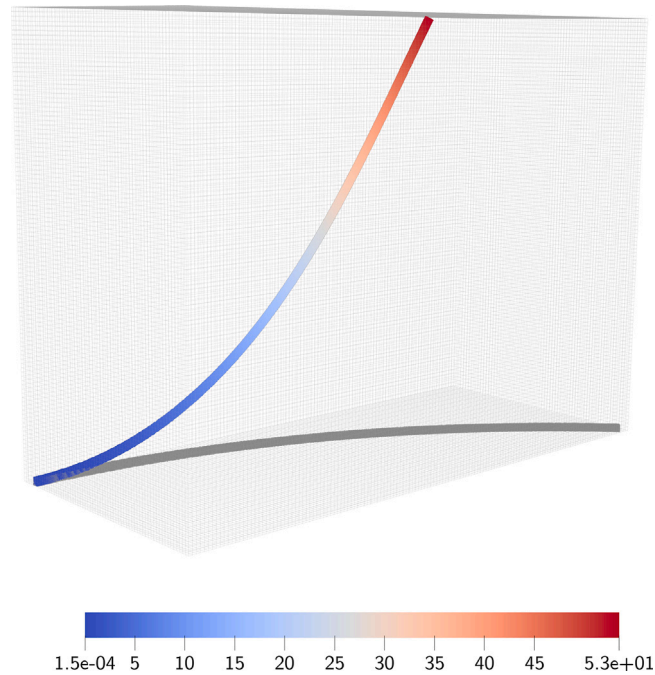
Fig. 12. Undeformed and final configurations of the MPM analysis with the $0.5 \times 0.5 \times 0.5$ mesh size, coloured according to $z-$displacement. (For interpretation of the references to colour in this figure legend, the reader is referred to the web version of this article.)

is likely due to poorly filled grid cells in the MPM contributing a lower stiffness than designed, leading to a larger displacement response than the equivalent FEA — the same effect achieved with reduced integration in the conventional FEM. As reflected in the listed CPU times, the MPM does require greater computational resources to analyse a similar mesh size as many more integration points must be iterated over, and an expensive element search must be conducted at the start of each loadstep to determine the locations of the material points relative to the grid. For this specific case, however, the MPM actually delivers a more accurate result with a coarser mesh in less time: for example, an error norm of 1.31 took the MPM just 792.7 s to produce, whereas the FEM result with an error norm of 1.75 took 5425.0 s – almost seven times as long. It must be emphasised here though that because the problems solved by the two implementations differ slightly, both from each other due to necessary differences in setup, and from the problem solved analytically in [67], any conclusions drawn from this comparison must not be taken as definitive or absolute. But this analysis does demonstrate that the MPM formulation is capable of handling large, three-dimensional rotations at least as competently as the FEM, and in some circumstances is able to deliver more accurate displacement results with a coarser mesh size, with a lower computational cost.

5. Conclusion

A new numerical framework for geometrically-exact micropolar elasticity has been presented. The non-linear kinematics are based on the work of Steinmann [31], Neff [32] and others and the constitutive laws are those used in classical micropolar elasticity for linear materials. Although the numerical implementation developed is an implicit MPM, qualifying this work particularly for large deformation problems, many aspects (for example, the consistent tangent or rotation update algorithm) could be used in an Updated Lagrangian FEM formulation.

The method was verified rigorously using the MMS, showing good convergence towards the analytical solutions and proving coercivity. Moreover the Newton–Raphson convergence was observed to be asymptotically quadratic, validating the consistent linearisation of the internal force and couple with respect to incremental deformations presented in Appendix A. The differing
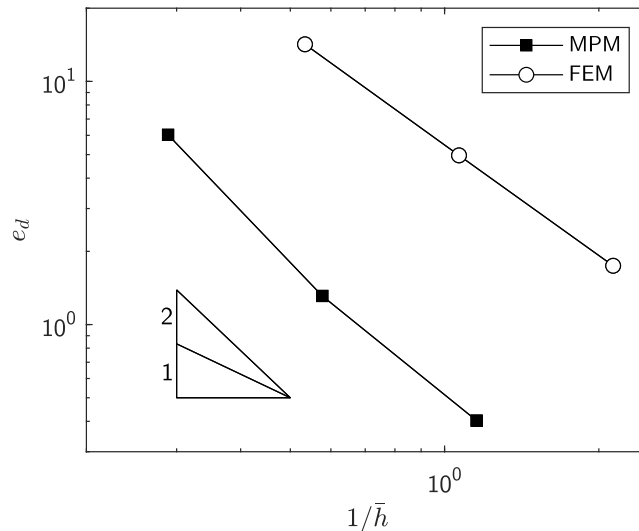
Fig. 13. Convergence of the displacement error norms for the FEM and MPM implementations with decreasing element size.

responses of two microscopic cantilevers with different characteristic bending lengths show that the method can simulate scenarios where the stiffness of a structure can be varied simply by modifying its size relative to its constituent microstructure. This is an important result as it demonstrates that the method has promise for modelling devices and structures exhibiting prominent size effects — something which conventional models cannot reproduce, yet is crucial for the accelerating industrial trend towards miniaturisation. A second numerical example showed torsion of a cantilever shaft beyond a full revolution without hitting any artificial limits on the rotation, or showing signs of any obvious ill conditioning of the system. The final example of a cantilever with an initial curvature also demonstrated a large rotation with a changing rotation axis. Together, these two examples prove that the method can robustly handle very large, three-dimensional rotations without encountering the difficulties or singularities suffered by some other formulations.

Although the number of benefits of a purely elastic micropolar MPM are perhaps limited, this work is a necessary stepping stone to any future, genuinely useful implementations. For example, the method could be extended to include elasto-plasticity, where size effects become even more pronounced, with subsequent application to geotechnical problems, for which micropolar theory and the MPM are both acknowledged to show particular promise. Other work may also like to focus on addressing the limitations of this contribution, particularly the issues surrounding the interpolated rotation and its associated path dependency.

Declaration of competing interest

The authors declare that they have no known competing financial interests or personal relationships that could have appeared to influence the work reported in this paper.

Data availability

Data will be made available on request.

Acknowledgements

Appendix A. Linearisation of internal force and couple

In this appendix, the analytical consistent linearisation of the internal force and couple vectors with respect to incremental deformations is presented as comprehensively as possible using index notation due to its highly intricate and tortuous nature. The following well-known results are used:

$$a_i \delta_{ij} = a_j \tag{A.1}$$

$$\frac{\partial a_{ij}}{\partial a_{kl}} = \delta_{ik}\delta_{jl} \tag{A.2}$$

$$\frac{\partial a_{ij}^{-1}}{\partial a_{kl}} = -a_{ik}^{-1}a_{lj}^{-1} \tag{A.3}$$

$$\frac{\partial \det(\boldsymbol{a})}{\partial a_{ij}} = \det(\boldsymbol{a})\, a_{ji}^{-1}. \tag{A.4}$$

For quantities described with both upper- and lower-case indices, e.g. $(\bullet)_{Aa}$, these refer to a node number and direction/component respectively.

A.1. Linearisation of internal force with respect to translations

Through application of the formula $\mathrm{d}\Omega = J\,\mathrm{d}\Omega_0$ and the chain rule,

$$K_{IiJj}^{pu} = \frac{\partial p_{Ii}^{\mathrm{int}}}{\partial u_{Jj}} \tag{A.5}$$

$$= \int_{\Omega_0} \frac{\partial}{\partial u_{Jj}}\left(\frac{\partial N_I}{\partial x_r}J\sigma_{ir}\right)\mathrm{d}\Omega_0 \tag{A.6}$$

$$= \int_{\Omega_0} \frac{\partial}{\partial F_{m\theta}}\left(\frac{\partial N_I}{\partial x_r}J\sigma_{ir}\right)\frac{\partial F_{m\theta}}{\partial u_{Jj}}\,\mathrm{d}\Omega_0 \tag{A.7}$$

$$= \int_{\Omega_0} \frac{\partial}{\partial F_{m\theta}}\left(\frac{\partial N_I}{\partial x_r}J\sigma_{ir}\right)\frac{\partial}{\partial u_{Jj}}\left(\frac{\partial(X_m+u_m)}{\partial X_\theta}\right)\mathrm{d}\Omega_0 \tag{A.8}$$

$$= \int_{\Omega_0} \frac{\partial}{\partial F_{m\theta}}\left(\frac{\partial N_I}{\partial x_r}J\sigma_{ir}\right)\frac{\partial}{\partial u_{Jj}}\left(\delta_{m\theta}+\frac{\partial(N_H u_{Hm})}{\partial X_\theta}\right)\mathrm{d}\Omega_0 \tag{A.9}$$

$$= \int_{\Omega_0} \frac{\partial}{\partial F_{m\theta}}\left(\frac{\partial N_I}{\partial x_r}J\sigma_{ir}\right)\frac{\partial(N_H\delta_{HJ}\delta_{jm})}{\partial X_\theta}\,\mathrm{d}\Omega_0 \tag{A.10}$$

$$= \int_{\Omega_0} \frac{\partial}{\partial F_{m\theta}}\left(\frac{\partial N_I}{\partial x_r}J\sigma_{ir}\right)\frac{\partial N_J}{\partial x_s}\frac{\partial x_s}{\partial X_\theta}\delta_{jm}\,\mathrm{d}\Omega_0 \tag{A.11}$$

$$= \int_{\Omega_0} \frac{\partial}{\partial F_{m\theta}}\left(\frac{\partial N_I}{\partial x_r}J\sigma_{ir}\right)\frac{\partial N_J}{\partial x_s}F_{s\theta}\delta_{jm}\,\mathrm{d}\Omega_0\,. \tag{A.12}$$

Then by the product rule

$$\frac{\partial}{\partial F_{m\theta}}\left(\frac{\partial N_I}{\partial x_r}J\sigma_{ir}\right) = \frac{\partial}{\partial F_{m\theta}}\left(\frac{\partial N_I}{\partial x_r}\right)J\sigma_{ir} + \frac{\partial N_I}{\partial x_r}\frac{\partial(J\sigma_{ir})}{\partial F_{m\theta}} \tag{A.13}$$

where

$$\frac{\partial}{\partial F_{m\theta}}\left(\frac{\partial N_I}{\partial x_r}\right) = \frac{\partial}{\partial F_{m\theta}}\left(\frac{\partial N_I}{\partial X_\rho}F_{\rho r}^{-1}\right) \tag{A.14}$$

$$= \frac{\partial N_I}{\partial X_s}\frac{\partial F_{\rho r}^{-1}}{\partial F_{m\theta}} \tag{A.15}$$

$$= -\frac{\partial N_I}{\partial X_\rho}F_{\rho m}^{-1}F_{\theta r}^{-1} \tag{A.16}$$

$$= -\frac{\partial N_I}{\partial x_m}F_{\theta r}^{-1} \tag{A.17}$$

such that (A.13) now becomes

$$\frac{\partial}{\partial F_{m\theta}}\left(\frac{\partial N_I}{\partial x_r}J\sigma_{ir}\right) = \frac{\partial N_I}{\partial x_r}\frac{\partial(J\sigma_{ir})}{\partial F_{m\theta}} - \frac{\partial N_I}{\partial x_m}J\sigma_{ir}F_{\theta r}^{-1}. \tag{A.18}$$

Meanwhile, substitution of the Biot-like stress definition (18), constitutive Eq. (20) and strain (8) leads to

$$\frac{\partial(J\sigma_{ir})}{\partial F_{m\theta}} = \frac{\partial}{\partial F_{m\theta}}\left(Q_{i\alpha}B_{\alpha\beta}F_{r\beta}\right) \tag{A.19}$$

$$= Q_{i\alpha}\left(\frac{\partial B_{\alpha\beta}}{\partial F_{m\theta}}F_{r\beta} + B_{\alpha\beta}\frac{\partial F_{r\beta}}{\partial F_{m\theta}}\right) \tag{A.20}$$

$$= Q_{i\alpha}\left(\frac{\partial}{\partial F_{m\theta}}\left(D_{\alpha\beta\gamma\pi}E_{\gamma\pi}\right)F_{r\beta} + B_{\alpha\beta}\delta_{rm}\delta_{\beta\theta}\right) \tag{A.21}$$

$$= Q_{i\alpha}\left(\frac{\partial}{\partial F_{m\theta}}\left(D_{\alpha\beta\gamma\pi}(Q_{i\gamma}F_{i\pi}-\delta_{\gamma\pi})\right)F_{r\beta} + B_{\alpha\theta}\delta_{rm}\right) \tag{A.22}$$

$$= Q_{i\alpha}\left(D_{\alpha\beta\gamma\pi}Q_{i\gamma}\frac{\partial F_{i\pi}}{\partial F_{m\theta}}F_{r\beta} + B_{\alpha\theta}\delta_{rm}\right) \tag{A.23}$$

$$= Q_{i\alpha} \left(D_{\alpha\beta\gamma\pi} Q_{i\gamma} \delta_{im} \delta_{\pi\theta} F_{r\beta} + B_{\alpha\theta} \delta_{rm} \right) \tag{A.24}$$

$$= Q_{i\alpha} \left(D_{\alpha\beta\gamma\theta} Q_{m\gamma} F_{r\beta} + B_{\alpha\theta} \delta_{rm} \right) \tag{A.25}$$

which can be substituted into (A.18) for

$$\frac{\partial}{\partial F_{m\theta}} \left(\frac{\partial N_I}{\partial x_r} J\sigma_{ir} \right) = \frac{\partial N_I}{\partial x_r} Q_{i\alpha} \left(D_{\alpha\beta\theta} Q_{m\gamma} F_{r\beta} + B_{\alpha\theta} \delta_{rm} \right) - \frac{\partial N_I}{\partial x_m} J\sigma_{ir} F_{\theta r}^{-1} \tag{A.26}$$

$$= \frac{\partial N_I}{\partial x_r} Q_{i\alpha} F_{r\beta} D_{\alpha\beta\gamma\theta} Q_{m\gamma} + \frac{\partial N_I}{\partial x_m} \left(Q_{i\alpha} B_{\alpha\theta} - J\sigma_{ir} F_{\theta r}^{-1} \right) \tag{A.27}$$

$$= \frac{\partial N_I}{\partial x_r} Q_{i\alpha} F_{r\beta} D_{\alpha\beta\gamma\theta} Q_{m\gamma} + \frac{\partial N_I}{\partial x_m} \left(Q_{i\alpha} B_{\alpha\theta} - J(J^{-1} Q_{i\alpha} B_{\alpha\beta} F_{r\beta}) F_{\theta r}^{-1} \right) \tag{A.28}$$

$$= \frac{\partial N_I}{\partial x_r} Q_{i\alpha} F_{r\beta} D_{\alpha\beta\gamma\theta} Q_{m\gamma} + \frac{\partial N_I}{\partial x_m} \left(Q_{i\alpha} B_{\alpha\theta} - Q_{i\alpha} B_{\alpha\theta} \right) \tag{A.29}$$

$$= \frac{\partial N_I}{\partial x_r} Q_{i\alpha} F_{r\beta} D_{\alpha\beta\gamma\theta} Q_{m\gamma} . \tag{A.30}$$

And finally, the expression for tangent stiffness is

$$K_{IiJj}^{pu} = \int_{\Omega_0} \frac{\partial N_I}{\partial x_r} Q_{i\alpha} F_{r\beta} D_{\alpha\beta\gamma\theta} Q_{m\gamma} \frac{\partial N_J}{\partial x_s} F_{s\theta} \delta_{jm} \, d\Omega_0 \tag{A.31}$$

$$= \int_{\Omega} \frac{\partial N_I}{\partial x_r} J^{-1} Q_{i\alpha} F_{r\beta} D_{\alpha\beta\gamma\theta} Q_{j\gamma} F_{s\theta} \frac{\partial N_J}{\partial x_s} \, d\Omega \tag{A.32}$$

$$= \int_{\Omega} \frac{\partial N_I}{\partial x_r} \mathrm{a}_{irjs}^{pu} \frac{\partial N_J}{\partial x_s} \, d\Omega \tag{A.33}$$

where

$$\mathrm{a}_{irjs}^{pu} = J^{-1} Q_{i\alpha} F_{r\beta} D_{\alpha\beta\gamma\theta} Q_{j\gamma} F_{s\theta} \tag{A.34}$$

$$= J^{-1} T_{ir\alpha\beta} D_{\alpha\beta\gamma\theta} T_{js\gamma\theta} \tag{A.35}$$

is the tangent modulus, with

$$T_{ir\alpha\beta} = Q_{i\alpha} F_{r\beta} . \tag{A.36}$$

A.2. Linearisation of internal force with respect to rotations

Since microrotations have no effect on volume change (i.e. $\frac{\partial J}{\partial w_s} = 0$), the evolution of the domain size need not be considered. Hence,

$$K_{IiJj}^{pw} = \frac{\partial p_{Ii}^{\mathrm{int}}}{\partial w_{Jj}} \tag{A.37}$$

$$= \int_{\Omega} \frac{\partial}{\partial w_{Jj}} \left(\frac{\partial N_I}{\partial x_r} \sigma_{ir} \right) d\Omega \tag{A.38}$$

$$= \int_{\Omega} \frac{\partial}{\partial Q_{m\theta}} \left(\frac{\partial N_I}{\partial x_r} \sigma_{ir} \right) \frac{\partial Q_{m\theta}}{\partial w_{Jj}} \, d\Omega \tag{A.39}$$

$$= \int_{\Omega} \frac{\partial N_I}{\partial x_r} \frac{\partial \sigma_{ir}}{\partial Q_{m\theta}} \frac{\partial Q_{m\theta}}{\partial w_s} \frac{\partial w_s}{\partial w_{Jj}} \, d\Omega \tag{A.40}$$

$$= \int_{\Omega} \frac{\partial N_I}{\partial x_r} \frac{\partial \sigma_{ir}}{\partial Q_{m\theta}} \frac{\partial Q_{m\theta}}{\partial w_s} \frac{\partial (N_H w_{Hs})}{\partial w_{Jj}} \, d\Omega \tag{A.41}$$

$$= \int_{\Omega} \frac{\partial N_I}{\partial x_r} \frac{\partial \sigma_{ir}}{\partial Q_{m\theta}} \frac{\partial Q_{m\theta}}{\partial w_s} \left(N_H \delta_{HJ} \delta_{sj} \right) d\Omega \tag{A.42}$$

$$= \int_{\Omega} \frac{\partial N_I}{\partial x_r} \frac{\partial \sigma_{ir}}{\partial Q_{m\theta}} \frac{\partial Q_{m\theta}}{\partial w_j} N_J \, d\Omega . \tag{A.43}$$

Then

$$\frac{\partial \sigma_{ir}}{\partial Q_{m\theta}} = \frac{\partial}{\partial Q_{m\theta}} \left(J^{-1} Q_{i\alpha} B_{\alpha\beta} F_{r\beta} \right) \tag{A.44}$$

$$= J^{-1} \left(\frac{\partial Q_{i\alpha}}{\partial Q_{m\theta}} B_{\alpha\beta} + Q_{i\alpha} \frac{\partial B_{\alpha\beta}}{\partial Q_{m\theta}} \right) F_{r\beta} \tag{A.45}$$

$$= J^{-1} \left(\delta_{im} \delta_{\alpha\theta} B_{\alpha\beta} + Q_{i\alpha} \frac{\partial}{\partial Q_{m\theta}} \left(D_{\alpha\beta\gamma\pi} E_{\gamma\pi} \right) \right) F_{r\beta} \tag{A.46}$$

$$= J^{-1} \left(\delta_{im} B_{\theta\beta} + Q_{i\alpha} D_{\alpha\beta\gamma\pi} \frac{\partial}{\partial Q_{m\theta}} \left(Q_{k\gamma} F_{k\pi} - \delta_{\gamma\pi} \right) \right) F_{r\beta} \tag{A.47}$$

$$= J^{-1} \left(\delta_{im} B_{\theta\beta} + Q_{i\alpha} D_{\alpha\beta\gamma\pi} \frac{\partial Q_{k\gamma}}{\partial Q_{m\theta}} F_{k\pi} \right) F_{r\beta} \tag{A.48}$$

$$= J^{-1} \left(\delta_{im} B_{\theta\beta} + Q_{i\alpha} D_{\alpha\beta\gamma\pi} \delta_{km} \delta_{\gamma\theta} F_{k\pi} \right) F_{r\beta} \tag{A.49}$$

$$= J^{-1} \delta_{im} B_{\theta\beta} F_{r\beta} + J^{-1} Q_{i\alpha} F_{r\beta} D_{\alpha\beta\theta\pi} F_{m\pi}. \tag{A.50}$$

The derivative of the microrotation tensor with respect to the spatial microrotation vector increment from the follower axes is obtained as (see Appendix B)

$$\frac{\partial Q_{m\theta}}{\partial w_j} = e_{mjn} Q_{n\theta} \tag{A.51}$$

which can be multiplied by (A.50) to give

$$\frac{\partial \sigma_{ir}}{\partial Q_{m\theta}} \frac{\partial Q_{m\theta}}{\partial w_j} = (J^{-1} \delta_{im} B_{\theta\beta} F_{r\beta} + J^{-1} Q_{i\alpha} F_{r\beta} D_{\alpha\beta\theta\pi} F_{m\pi}) e_{mjn} Q_{n\theta} \tag{A.52}$$

$$= (J^{-1} \delta_{im} Q_{n\theta} B_{\theta\beta} F_{r\beta} + J^{-1} Q_{i\alpha} F_{r\beta} D_{\alpha\beta\theta\pi} Q_{n\theta} F_{m\pi}) e_{mjn} \tag{A.53}$$

$$= (\delta_{im} \sigma_{nr} + J^{-1} Q_{i\alpha} F_{r\beta} D_{\alpha\beta\theta\pi} Q_{n\theta} F_{m\pi}) e_{mjn} \tag{A.54}$$

to be substituted into (A.43) for

$$K_{IiJj}^{pw} = \int_\Omega \frac{\partial N_I}{\partial x_r} \left(J^{-1} Q_{i\alpha} F_{r\beta} D_{\alpha\beta\theta\pi} Q_{n\theta} F_{m\pi} + \delta_{im} \sigma_{nr} \right) e_{mjn} N_J \, d\Omega \tag{A.55}$$

$$= \int_\Omega \frac{\partial N_I}{\partial x_r} \mathrm{a}_{irnm}^{pw} e_{nmj} N_J \, d\Omega. \tag{A.56}$$

Conveniently,

$$\mathrm{a}_{irnm}^{pw} = \mathrm{a}_{irnm}^{pu} + \delta_{im} \sigma_{nr}. \tag{A.57}$$

A.3. Linearisation of internal couple with respect to translations

$$K_{IiJj}^{mu} = \frac{\partial m_{Ii}^{\mathrm{int}}}{\partial u_{Jj}} \tag{A.58}$$

$$= \int_\Omega \frac{\partial}{\partial u_{Jj}} \left(\frac{\partial N_I}{\partial x_r} \mu_{ir} + N_I e_{irn} \sigma_{rn} \right) d\Omega \tag{A.59}$$

$$= \int_{\Omega_0} \frac{\partial}{\partial u_{Jj}} \left(\frac{\partial N_I}{\partial x_r} J \mu_{ir} + N_I e_{irn} J \sigma_{rn} \right) d\Omega_0 \tag{A.60}$$

$$= \int_{\Omega_0} \frac{\partial}{\partial F_{m\theta}} \left(\frac{\partial N_I}{\partial x_r} J \mu_{ir} + N_I e_{irn} J \sigma_{rn} \right) \frac{\partial F_{m\theta}}{\partial u_{Jj}} d\Omega_0 \tag{A.61}$$

$$= \int_{\Omega_0} \frac{\partial}{\partial F_{m\theta}} \left(\frac{\partial N_I}{\partial x_r} J \mu_{ir} + N_I e_{irn} J \sigma_{rn} \right) \frac{\partial N_J}{\partial x_s} F_{s\theta} \delta_{jm} d\Omega_0 \tag{A.62}$$

$$= \int_{\Omega_0} \left(\frac{\partial}{\partial F_{j\theta}} \left(\frac{\partial N_I}{\partial x_r} J \mu_{ir} \right) + N_I e_{irn} \frac{\partial (J \sigma_{rn})}{\partial F_{j\theta}} \right) \frac{\partial N_J}{\partial x_s} F_{s\theta} d\Omega_0 \tag{A.63}$$

where, following (A.18),

$$\frac{\partial}{\partial F_{j\theta}} \left(\frac{\partial N_I}{\partial x_r} J \mu_{ir} \right) = \frac{\partial N_I}{\partial x_r} \frac{\partial (J \mu_{ir})}{\partial F_{j\theta}} - \frac{\partial N_I}{\partial x_j} J \mu_{ir} F_{\theta r}^{-1}. \tag{A.64}$$

Using the definition of Biot-like couple-stress (19),

$$\frac{\partial (J \mu_{ir})}{\partial F_{j\theta}} = \frac{\partial}{\partial F_{j\theta}} \left(Q_{i\alpha} S_{\alpha\beta} F_{r\beta} \right) \tag{A.65}$$

$$= Q_{i\alpha} S_{\alpha\beta} \frac{\partial F_{r\beta}}{\partial F_{j\theta}} \tag{A.66}$$

$$= Q_{i\alpha} S_{\alpha\beta} \delta_{rj} \delta_{\beta\theta} \tag{A.67}$$

$$= Q_{i\alpha} S_{\alpha\theta} \delta_{rj} \tag{A.68}$$

so that (A.64) becomes

$$\frac{\partial}{\partial F_{j\theta}} \left(\frac{\partial N_I}{\partial x_r} J \mu_{ir} \right) = \frac{\partial N_I}{\partial x_r} Q_{i\alpha} S_{\alpha\theta} \delta_{rj} - \frac{\partial N_I}{\partial x_j} J \mu_{ir} F_{\theta r}^{-1} \tag{A.69}$$

$$= \frac{\partial N_I}{\partial x_j} \left(Q_{i\alpha} S_{\alpha\theta} - J \mu_{ir} F_{\theta r}^{-1} \right) \tag{A.70}$$

$$= \frac{\partial N_I}{\partial x_j} \left(J \mu_{ir} F_{\theta r}^{-1} - J \mu_{ir} F_{\theta r}^{-1} \right) \tag{A.71}$$

$$= 0. \tag{A.72}$$

From (A.63), and using (A.25),

$$N_I e_{irn} \frac{\partial (J \sigma_{rn})}{\partial F_{j\theta}} F_{s\theta} = N_I e_{irn} \left(Q_{r\alpha} \left(D_{\alpha\beta\gamma\theta} Q_{j\gamma} F_{n\beta} + B_{\alpha\theta} \delta_{nj} \right) \right) F_{s\theta} \tag{A.73}$$

$$= N_I e_{irn} \left(Q_{r\alpha} F_{n\beta} D_{\alpha\beta\gamma\theta} Q_{j\gamma} F_{s\theta} + Q_{r\alpha} B_{\alpha\theta} \delta_{nj} F_{s\theta} \right) \tag{A.74}$$

$$= N_I e_{irn} \left(Q_{r\alpha} F_{n\beta} D_{\alpha\beta\gamma\theta} Q_{j\gamma} F_{s\theta} + J \delta_{nj} \sigma_{rs} \right) \tag{A.75}$$

and, putting everything together,

$$K_{IiJj}^{mu} = \int_{\Omega} \left(N_I e_{irn} \left(Q_{r\alpha} F_{n\beta} D_{\alpha\beta\gamma\theta} Q_{j\gamma} F_{s\theta} + J \delta_{nj} \sigma_{rs} \right) \right) \frac{\partial N_J}{\partial x_s} \, \mathrm{d}\Omega_0 \tag{A.76}$$

$$= \int_{\Omega} \left(N_I e_{irn} \left(J^{-1} Q_{r\alpha} F_{n\beta} D_{\alpha\beta\gamma\theta} Q_{j\gamma} F_{s\theta} + \delta_{nj} \sigma_{rs} \right) \right) \frac{\partial N_J}{\partial x_s} \, \mathrm{d}\Omega \tag{A.77}$$

$$= \int_{\Omega} N_I e_{irn} \mathrm{a}_{rnjs}^{mu} \frac{\partial N_J}{\partial x_s} \, \mathrm{d}\Omega \tag{A.78}$$

and

$$\mathrm{a}_{rnjs}^{mu} = \mathrm{a}_{jsrn}^{pw}. \tag{A.79}$$

A.4. Linearisation of internal couple with respect to rotations

$$K_{IiJj}^{mw} = \frac{\partial m_{Ii}^{\mathrm{int}}}{\partial w_{Jj}} \tag{A.80}$$

$$= \int_{\Omega} \frac{\partial}{\partial w_{Jj}} \left(\frac{\partial N_I}{\partial x_r} \mu_{ir} + N_I e_{irn} \sigma_{rn} \right) \mathrm{d}\Omega \tag{A.81}$$

$$= \int_{\Omega} \left(\frac{\partial N_I}{\partial x_r} \frac{\partial \mu_{ir}}{\partial w_{Jj}} + N_I e_{irn} \frac{\partial \sigma_{rn}}{\partial Q_{m\theta}} \frac{\partial Q_{m\theta}}{\partial w_{Jj}} \right) \mathrm{d}\Omega. \tag{A.82}$$

Then,

$$\frac{\partial \mu_{ir}}{\partial w_{Jj}} = \frac{\partial}{\partial w_{Jj}} \left(J^{-1} Q_{i\alpha} S_{\alpha\beta} F_{r\beta} \right) \tag{A.83}$$

$$= J^{-1} \left(\frac{\partial Q_{i\alpha}}{\partial w_{Jj}} S_{\alpha\beta} + Q_{i\alpha} \frac{\partial S_{\alpha\beta}}{\partial w_{Jj}} \right) F_{r\beta} \tag{A.84}$$

where

$$\frac{\partial Q_{i\alpha}}{\partial w_{Jj}} = \frac{\partial Q_{i\alpha}}{\partial w_s} \frac{\partial w_s}{\partial w_{Jj}} \tag{A.85}$$

$$= (e_{isn} Q_{n\alpha}) \frac{\partial N_H w_{Hs}}{\partial w_{Jj}} \tag{A.86}$$

$$= Q_{n\alpha} e_{ijn} N_J \tag{A.87}$$

and

$$\frac{\partial S_{\alpha\beta}}{\partial w_{Jj}} = \frac{\partial}{\partial w_{Jj}} \left(\tilde{D}_{\alpha\beta\gamma\pi} \Gamma_{\gamma\pi} \right) \tag{A.88}$$

$$= \tilde{D}_{\alpha\beta\gamma\pi} \frac{\partial \Gamma_{\gamma\pi}}{\partial w_{Jj}} \tag{A.89}$$

which are substituted back into (A.84) to give

$$\frac{\partial \mu_{ir}}{\partial w_{Jj}} = J^{-1} \left(Q_{n\alpha} S_{\alpha\beta} e_{ijn} N_J + Q_{i\alpha} \tilde{D}_{\alpha\beta\gamma\pi} \frac{\partial \Gamma_{\gamma\pi}}{\partial w_{Jj}} \right) F_{r\beta} \tag{A.90}$$

$$= \mu_{nr} e_{ijn} N_J + J^{-1} Q_{i\alpha} F_{r\beta} \tilde{D}_{\alpha\beta\gamma\pi} \frac{\partial \Gamma_{\gamma\pi}}{\partial w_{Jj}}. \tag{A.91}$$

A discretisation of the Gâteaux derivative of the wryness tensor [57],

$$\delta \Gamma_{\gamma\pi} = Q_{j\gamma} \frac{\partial (\delta w_j)}{\partial X_{\pi}} \tag{A.92}$$

$$= Q_{j\gamma} \frac{\partial (N_J \delta w_{Jj})}{\partial X_\pi} \tag{A.93}$$

$$= Q_{j\gamma} \frac{\partial N_J}{\partial X_\pi} \delta w_{Jj} \tag{A.94}$$

can be rearranged to yield the straightforward result

$$\frac{\partial \Gamma_{\gamma\pi}}{\partial w_{Jj}} = Q_{j\gamma} \frac{\partial N_J}{\partial X_\pi} = Q_{j\gamma} \frac{\partial N_J}{\partial x_n} F_{n\pi} \tag{A.95}$$

so that (A.91) becomes

$$\frac{\partial \mu_{ij}}{\partial w_{Jj}} = \mu_{nr} e_{ijn} N_J + J^{-1} Q_{i\alpha} F_{r\beta} \tilde{D}_{\alpha\beta\gamma\pi} Q_{j\gamma} F_{n\pi} \frac{\partial N_J}{\partial x_n}. \tag{A.96}$$

Combining this with result (A.54) and substituting into (A.82) gives

$$\begin{aligned} K_{IiJj}^{mw} &= \int_\Omega \Bigg(N_I e_{irn} \left(\delta_{rm} \sigma_{sn} + J^{-1} Q_{r\alpha} F_{n\beta} D_{\alpha\beta\gamma\pi} Q_{s\gamma} F_{m\pi} \right) e_{mjs} N_J \\ &\quad + \frac{\partial N_I}{\partial x_r} \left(J^{-1} Q_{i\alpha} F_{r\beta} \tilde{D}_{\alpha\beta\gamma\pi} Q_{j\gamma} F_{n\pi} \frac{\partial N_J}{\partial x_n} + \mu_{nr} e_{ijn} N_J \right) \Bigg) \, d\Omega \end{aligned} \tag{A.97}$$

$$= \int_\Omega \left(N_I e_{irn} a_{rnsm}^{mw1} e_{smj} N_J + \frac{\partial N_I}{\partial x_r} \left(a_{irjn}^{mw2} \frac{\partial N_J}{\partial x_n} + a_{irns}^{mw3} e_{nsj} N_J \right) \right) \, d\Omega \tag{A.98}$$

where

$$a_{rnsm}^{mw1} = a_{rnsm}^{pw} \tag{A.99}$$

$$a_{irjn}^{mw2} = J^{-1} T_{ir\alpha\beta} \tilde{D}_{\alpha\beta\gamma\pi} T_{jn\gamma\pi} \tag{A.100}$$

$$a_{irns}^{mw3} = \delta_{is} \mu_{nr}. \tag{A.101}$$

Appendix B. Partial derivative of the microrotation tensor with respect to the spatial microrotation vector

The first variation of the microrotation tensor δQ in the direction of an incremental rotation δw is obtained by taking the Gâteaux derivative

$$\delta Q = \frac{d}{d\epsilon} \left((\Delta Q) Q \right) |_{\epsilon=0} \tag{B.1}$$

$$= \frac{d}{d\epsilon} \left(\exp \left(\epsilon \widehat{\delta w} \right) Q \right) |_{\epsilon=0} \tag{B.2}$$

$$= \widehat{\delta w} \exp \left(\epsilon \widehat{\delta w} \right) Q |_{\epsilon=0} \tag{B.3}$$

$$= \widehat{\delta w} Q \tag{B.4}$$

which in index notation is

$$Q_{m\theta} = e_{mjn} (\delta w_j) Q_{n\theta}. \tag{B.5}$$

This implies the partial derivative

$$\frac{\partial Q_{m\theta}}{\partial w_j} = e_{mjn} Q_{n\theta}. \tag{B.6}$$

References

[1] L. An, D. Zhang, L. Zhang, G. Feng, Effect of nanoparticle size on the mechanical properties of nanoparticle assemblies, Nanoscale 11 (19) (2019) 9563–9573.

[2] E. Arzt, Size effects in materials due to microstructural and dimensional constraints: a comparative review, Acta Mater. 46 (16) (1998) 5611–5626.

[3] I. Jasiuk, M. Ostoja-Starzewski, From lattices and composites to micropolar continua: Analysis of materials with complex microstructure, in: V.M. Harik, L.-S. Luo (Eds.), Micromechanics and Nanoscale Effects: MEMS, Multi-Scale Materials and Micro-Flows, Kluwer Academic Publishers, Netherlands, 2004, pp. 175–212.

[4] W. Voigt, Theoretische Studien über die Elastizitätsverhältnisse der Krystalle, in: Abhandlungen der Königlichen Gesellschaft der Wissenschaften in Göttingen, Dieterichsche Verlags-Buchhandlung, 1887.

[5] G. Hamel, Elementare mechanik, ein lehrbuch enthaltend: eine begründung der allgemeinen mechanik; die mechanik der systeme starrer körper: die synthetischen und die elemente der analytischen methoden, sowie eine einführung in die prizipien der mechanik deformierbarer system, B.G. Teubner, 1912.

[6] E. Cosserat, F. Cosserat, Théorie des corps déformables, A. Hermann et fils, Paris, 1909.

[7] R.D. Mindlin, Influence of Couple-Stresses on Stress Concentrations, Tech. Rep., Columbia Univ., New York, USA, 1962.

[8] R.D. Mindlin, Stress functions for a Cosserat continuum, Int. J. Solids Struct. 1 (3) (1965) 265–271.

[9] H. Neuber, On the general solution of linear-elastic problems in isotropic and anisotropic Cosserat continua, in: H. Görtler (Ed.), Applied Mechanics, Springer Berlin Heidelberg, Berlin, Heidelberg, 1966, pp. 153–158.

[10] A.C. Eringen, Linear theory of micropolar elasticity, J. Math. Mech. 15 (6) (1966) 909–923.

[11] S. Cowin, Stress functions for Cosserat elasticity, Int. J. Solids Struct. 6 (4) (1970) 389–398.

[12] H.-B. Mühlhaus, I. Vardoulakis, The thickness of shear bands in granular materials, Géotechnique 37 (3) (1987) 271–283.

[13] R. Lakes, Physical meaning of elastic constants in Cosserat, void, and microstretch elasticity, J. Mech. Mater. Struct. 11 (3) (2016) 217–229.

[14] N. Auffray, R. Bouchet, Y. Brechet, Strain gradient elastic homogenization of bidimensional cellular media, Int. J. Solids Struct. 47 (13) (2010) 1698–1710.

[15] D. Bigoni, W.J. Drugan, Analytical derivation of cosserat moduli via homogenization of heterogeneous elastic materials, J. Appl. Mech. 74 (4) (2007) 741–753.

[16] G. Rizzi, F. Dal Corso, D. Veber, D. Bigoni, Identification of second-gradient elastic materials from planar hexagonal lattices. Part II: Mechanical characteristics and model validation, Int. J. Solids Struct. 176 (2019) 19–35.

[17] J. Desrues, E. Andò, Strain localisation in granular media, C. R. Phys. 16 (1) (2015) 26–36.

[18] R. de Borst, Simulation of strain localization: A reappraisal of the Cosserat continuum, Eng. Comput. 8 (1991) 317–332.

[19] R. de Borst, L. Sluys, Localisation in a cosserat continuum under static and dynamic loading conditions, Comput. Methods Appl. Mech. Engrg. 90 (1–3) (1991) 805–827.

[20] F.-Y. Huang, L. Keo-Zoo, Torsional analysis of micropolar elasticity using the finite element method, Internat. J. Engrg. Sci. 32 (2) (1994) 347–358.

[21] S. Nakamura, R. Lakes, Finite element analysis of saint-venant end effects in micropolar elastic solids, Eng. Comput. 12 (6) (1995) 571–587.

[22] F.-Y. Huang, B.-H. Yan, J.-L. Yan, D.-U. Yang, Bending analysis of micropolar elastic beam using a 3-D finite element method, Internat. J. Engrg. Sci. 38 (3) (2000) 275–286.

[23] E. Providas, M. Kattis, Finite element method in plane Cosserat elasticity, Comput. Struct. 80 (27) (2002) 2059–2069.

[24] H. Zhang, H. Wang, G. Liu, Quadrilateral isoparametric finite elements for plane elastic Cosserat bodies, Acta Mech. Sin. 21 (4) (2005) 388–394.

[25] A. Khoei, S. Yadegari, S. Biabanaki, 3D finite element modeling of shear band localization via the micro-polar Cosserat continuum theory, Comput. Mater. Sci. 49 (4) (2010) 720–733.

[26] S. Bauer, W. Dettmer, D. Perić, M. Schäfer, Micropolar hyperelasticity: constitutive model, consistent linearization and simulation of 3D scale effects, Comput. Mech. 50 (2012) 383–396.

[27] S. Bauer, W. Dettmer, D. Perić, M. Schäfer, Micropolar hyper-elastoplasticity: constitutive model, consistent linearization, and simulation of 3D scale effects, Internat. J. Numer. Methods Engrg. 91 (1) (2012) 39–66.

[28] S.G. Erdelj, G. Jelenić, A. Ibrahimbegović, Geometrically non-linear 3D finite-element analysis of micropolar continuum, Int. J. Solids Struct. 202 (2020) 745–764.

[29] S. Bauer, M. Schäfer, P. Grammenoudis, C. Tsakmakis, Three-dimensional finite elements for large deformation micropolar elasticity, Comput. Methods Appl. Mech. Engrg. 199 (41–44) (2010) 2643–2654.

[30] P. Grammenoudis, C. Tsakmakis, Finite element implementation of large deformation micropolar plasticity exhibiting isotropic and kinematic hardening effects, Internat. J. Numer. Methods Engrg. 62 (12) (2005) 1691–1720.

[31] P. Steinmann, A micropolar theory of finite deformation and finite rotation multiplicative elastoplasticity, Int. J. Solids Struct. 31 (8) (1994) 1063–1084.

[32] P. Neff, A finite-strain elastic–plastic Cosserat theory for polycrystals with grain rotations, Internat. J. Engrg. Sci. 44 (8–9) (2006) 574–594.

[33] A.C. Eringen, Microcontinuum Field Theories: I. Foundations and Solids, Springer Science & Business Media, 2012.

[34] T. Belytschko, W.K. Liu, B. Moran, K. Elkhodary, Nonlinear Finite Elements for Continua and Structures, second ed., John Wiley & Sons, 2014.

[35] D. Sulsky, Z. Chen, H.L. Schreyer, A particle method for history-dependent materials, Comput. Methods Appl. Mech. Engrg. 118 (1–2) (1994) 179–196.

[36] A. Stomakhin, C. Schroeder, L. Chai, J. Teran, A. Selle, A material point method for snow simulation, ACM Trans. Graph. 32 (4) (2013) 1–10.

[37] K. Soga, E. Alonso, A. Yerro, K. Kumar, S. Bandara, Trends in large-deformation analysis of landslide mass movements with particular emphasis on the material point method, Géotechnique 66 (3) (2016) 248–273.

[38] J. Gaume, A.M. Puzrin, Mechanisms of slab avalanche release and impact in the Dyatlov Pass incident in 1959, Commun. Earth Environ. 2 (1) (2021) 1–11.

[39] S.G. Bardenhagen, E.M. Kober, The generalized interpolation material point method, CMES Comput. Model. Eng. Sci. 5 (6) (2004) 477–496.

[40] T.J. Charlton, W.M. Coombs, C.E. Augarde, iGIMP: An implicit generalised interpolation material point method for large deformations, Comput. Struct. 190 (2017) 108–125.

[41] F. Dufour, H.-B. Mühlhaus, L. Moresi, A particle-in-cell formulation for large deformation in Cosserat continua, in: Bifurcation and Localisation Theory in Geomechanics, CRC Press, 2001, pp. 133–138.

[42] R. Ma, W. Sun, A finite micro-rotation material point method for micropolar solid and fluid dynamics with three-dimensional evolving contacts and free surfaces, Comput. Methods Appl. Mech. Engrg. 391 (2022) 114540.

[43] J.E. Guilkey, J.A. Weiss, Implicit time integration for the material point method: Quantitative and algorithmic comparisons with the finite element method, Internat. J. Numer. Methods Engrg. 57 (9) (2003) 1323–1338.

[44] T.J. O'Hare, P.A. Gourgiotis, W.M. Coombs, C.E. Augarde, A geometrically-exact Finite Element Method for micropolar continua with finite deformations, UKACM, 2023.

[45] W.M. Coombs, C.E. Augarde, A.J. Brennan, M.J. Brown, T.J. Charlton, J.A. Knappett, Y.G. Motlagh, L. Wang, On Lagrangian mechanics and the implicit material point method for large deformation elasto-plasticity, Comput. Methods Appl. Mech. Engrg. 358 (2020) 112622.

[46] L. Euler, Découverte d'un nouveau principe de mécanique, Mém. Acad. Sci. Berlin (1752) 185–217.

[47] J. Argyris, An excursion into large rotations, Comput. Methods Appl. Mech. Engrg. 32 (1) (1982) 85–155.

[48] R. Brannon, Rotation, Reflection, and Frame Changes: Orthogonal Tensors in Computational Engineering Mechanics, IOP Publishing, 2018, Orthogonal tensors in computational engineering mechanics.

[49] K. Shoemake, Animating rotation with quaternion curves, in: Proceedings of the 12th Annual Conference on Computer Graphics and Interactive Techniques, 1985, pp. 245–254.

[50] A. Ibrahimbegović, On the choice of finite rotation parameters, Comput. Methods Appl. Mech. Engrg. 149 (1) (1997) 49–71.

[51] A.C. Eringen, Continuum physics. Volume 4-polar and nonlocal field theories, 1976, New York.

[52] W. Pietraszkiewicz, V. Eremeyev, On natural strain measures of the non-linear micropolar continuum, Int. J. Solids Struct. 46 (3–4) (2009) 774–787.

[53] P. Neff, M. Bîrsan, F. Osterbrink, Existence theorem for geometrically nonlinear Cosserat micropolar model under uniform convexity requirements, J. Elasticity 121 (1) (2015) 119–141.

[54] S. Hassanpour, G.R. Heppler, Micropolar elasticity theory: a survey of linear isotropic equations, representative notations, and experimental investigations, Math. Mech. Solids 22 (2) (2017) 224–242.

[55] R.A. Toupin, Theories of elasticity with couple-stress, Arch. Ration. Mech. Anal. 17 (2) (1964) 85–112.

[56] W.M. Coombs, C.E. Augarde, AMPLE: A material point learning environment, Adv. Eng. Softw. 139 (102748) (2020).

[57] C. Sansour, W. Wagner, Multiplicative updating of the rotation tensor in the finite element analysis of rods and shells – a path independent approach, Comput. Mech. 31 (2003) 153–162.

[58] G. Jelenić, M. Crisfield, Geometrically exact 3D beam theory: implementation of a strain-invariant finite element for statics and dynamics, Comput. Methods Appl. Mech. Engrg. 171 (1) (1999) 141–171.

[59] A. Ibrahimbegović, I. Kožar, Non-linear Wilson's brick element for finite elastic deformations of three-dimensional solids, Commun. Numer. Methods. Eng. 11 (1995) 655–664.

[60] A. Ibrahimbegović, F. Frey, I. Kožar, Computational aspects of vector-like parametrization of three-dimensional finite rotations, Internat. J. Numer. Methods Engrg. 38 (21) (1995) 3653–3673.

[61] G. Jelenić, Pure bending in non-linear micropolar elasticity, Int. J. Mech. Mater. Des. 18 (1) (2022) 243–265.
[62] Y. Bing, M. Cortis, T.J. Charlton, W.M. Coombs, C.E. Augarde, B-spline based boundary conditions in the material point method, Comput. Struct. 212 (2019) 257–274.
[63] E.A. de Souza Neto, D. Peric, D.R. Owen, Computational Methods for Plasticity: Theory and Applications, John Wiley & Sons, 2011.
[64] N. Fleck, G. Muller, M. Ashby, J. Hutchinson, Strain gradient plasticity: Theory and experiment, Acta Metall. Mater. 42 (2) (1994) 475–487.
[65] J. Stölken, A. Evans, A microbend test method for measuring the plasticity length scale, Acta Mater. 46 (14) (1998) 5109–5115.
[66] K.-J. Bathe, S. Bolourchi, Large displacement analysis of three-dimensional beam structures, Internat. J. Numer. Methods Engrg. 14 (7) (1979) 961–986.
[67] I. Kožar, A. Ibrahimbegović, Finite element formulation of the finite rotation solid element, Finite Elem. Anal. Des. 20 (2) (1995) 101–126.